

# A monocyte–leptin–angiogenesis pathway critical for repair post-infection

<https://doi.org/10.1038/s41586-022-05044-x>

Received: 11 June 2021

Accepted: 29 June 2022

Published online: 10 August 2022

 Check for updates

Rachel M. Kratošil<sup>1,2</sup>, Hanjoo B. Shim<sup>1,2</sup>, Raymond Shim<sup>1,2</sup>, Woo Yong Lee<sup>1,2</sup>, Elodie Labit<sup>3,4</sup>, Sarthak Sinha<sup>3,4</sup>, Catherine M. Keenan<sup>1,2,5</sup>, Bas G. J. Surewaard<sup>1,2</sup>, Ji Yeon Noh<sup>6</sup>, Yuxiang Sun<sup>6</sup>, Keith A. Sharkey<sup>1,2,5</sup>, Matthias Mack<sup>7</sup>, Jeff Biernaskie<sup>3,4,5,8</sup>, Justin F. Deniset<sup>1,2,9,10,11</sup> & Paul Kubes<sup>1,2,11</sup>✉

During infection, inflammatory monocytes are thought to be key for bacterial eradication, but this is hard to reconcile with the large numbers of neutrophils that are recruited for each monocyte that migrates to the afflicted tissue, and the much more robust microbicidal functions of the neutrophils. However, unlike neutrophils, monocytes have the capacity to convert to situationally specific macrophages that may have critical functions beyond infection control<sup>1,2</sup>. Here, using a foreign body coated with *Staphylococcus aureus* and imaging over time from cutaneous infection to wound resolution, we show that monocytes and neutrophils are recruited in similar numbers with low-dose infection but not with high-dose infection, and form a localization pattern in which monocytes surround the infection site, whereas neutrophils infiltrate it. Monocytes did not contribute to bacterial clearance but converted to macrophages that persisted for weeks after infection, regulating hypodermal adipocyte expansion and production of the adipokine hormone leptin. In infected monocyte-deficient mice there was increased persistent hypodermis thickening and an elevated leptin level, which drove overgrowth of dysfunctional blood vasculature and delayed healing, with a thickened scar. Ghrelin, which opposes leptin function<sup>3</sup>, was produced locally by monocytes, and reduced vascular overgrowth and improved healing post-infection. In sum, we find that monocytes function as a cellular rheostat by regulating leptin levels and revascularization during wound repair.

Immune cells must carefully choreograph microbicidal activity (inflammation) with wound repair (resolution and anti-inflammation). During infection, neutrophils are first to arrive in large numbers and attempt to eradicate the bacteria. Monocytes enter shortly thereafter<sup>4</sup> and are thought to help contain and/or eradicate the infection, and finally, macrophages help to repair the wound. The loss of neutrophils is sufficient to cause severe disease<sup>5</sup>, whereas the role of the other cells is less well understood. Information derived from static histological data suggests that monocytes and macrophages are indeed present at sites of bacterial infection<sup>6–8</sup>. *S. aureus* infections are a severe and common clinical problem. Here we used a model of low-dose *S. aureus* infection that boosted the number of infiltrating monocytes to similar levels as neutrophils, and by visualizing these cells over time, we observed zonation of the monocytes around the infectious nidus and their conversion to macrophages that were critical for repair but not required to mitigate the infection. Unexpectedly, the monocyte/macrophage lineage regulated fat cell expansion and subsequent angiogenesis through leptin

and its counteracting hormone ghrelin, processes that are critical for wound repair. Whereas monocytes–macrophages have previously been shown to help in vascular growth<sup>9</sup>, here we showed that they also have the capacity to regulate and limit excessive vascular growth. This work has broad implications for wound repair as well as potentially for cancer, fibrosis and metabolic diseases.

## Increased monocytes in low-dose skin infection

Skin damage associated with foreign bodies (such as splinters, shards of glass and medical devices) are the most common route for pathogens to penetrate into the subcutaneous layer of the skin and persist, leading to serious infections, such as *S. aureus*. The foreign body provides a platform for biofilm formation, which subverts immunity and is the scenario most commonly encountered in hospitals<sup>10</sup>. Around 80% of studies of skin infection by *S. aureus* use a high to very high infectious inoculum in planktonic form (Extended Data Fig. 1a–c),

<sup>1</sup>Department of Physiology and Pharmacology, Cumming School of Medicine, University of Calgary, Calgary, Alberta, Canada. <sup>2</sup>Calvin, Phoebe and Joan Snyder Institute for Chronic Diseases, Cumming School of Medicine, University of Calgary, Calgary, Alberta, Canada. <sup>3</sup>Department of Comparative Biology and Experimental Medicine, Faculty of Veterinary Medicine, University of Calgary, Calgary, Alberta, Canada. <sup>4</sup>Alberta Children's Hospital Research Institute, Cumming School of Medicine, University of Calgary, Calgary, Alberta, Canada. <sup>5</sup>Hotchkiss Brain Institute, Cumming School of Medicine, University of Calgary, Calgary, Alberta, Canada. <sup>6</sup>Department of Nutrition, Texas A&M University, College Station, TX, USA. <sup>7</sup>Department of Internal Medicine II - Nephrology, University Hospital Regensburg, Regensburg, Germany. <sup>8</sup>Department of Surgery, Cumming School of Medicine, University of Calgary, Calgary, Alberta, Canada. <sup>9</sup>Department of Cardiac Sciences, Cumming School of Medicine, University of Calgary, Calgary, Alberta, Canada. <sup>10</sup>Libin Cardiovascular Institute, Cumming School of Medicine, University of Calgary, Calgary, Alberta, Canada. <sup>11</sup>These authors contributed equally: Justin F. Deniset, Paul Kubes. ✉e-mail: [jdeniset@ucalgary.ca](mailto:jdeniset@ucalgary.ca); [pkubes@ucalgary.ca](mailto:pkubes@ucalgary.ca)

whereas a clinical infection is most likely to start with very low levels of bacteria on a foreign body. We thus developed a foreign body *S. aureus* model with these characteristics. We systematically reduced the concentration of bacteria from  $10^7$  to 500 colony-forming units (CFU) per bead and observed marked differences in the immune response. We observed a progressive change in myeloid cell recruitment ratios (Fig. 1c,d) favouring monocyte recruitment. Mice infected with one bead coated with *S. aureus* USA400 MW2 (500 CFU per bead) developed an active infection that lasted for a minimum of 7 days, whereas those infected with 500 CFU of *S. aureus* in suspension cleared the infection much more quickly (Extended Data Fig. 1d,e). The persistent nature of the infection from the *S. aureus*-coated bead had the appearance of biofilm formation, as assessed by electron microscopy (Extended Data Fig. 1f). Additionally, *S. aureus* from the bead disseminated to the skin-draining lymph nodes at 72 h after infection, with a small percentage of mice exhibiting bacterial dissemination to peripheral organs such as the kidney and liver, which is not observed in planktonic infection (Extended Data Fig. 1g).

Using multiphoton intravital microscopy, we performed real-time in vivo imaging of the infection site using double-reporter *Cx3cr1<sup>GFP/+</sup>* Catchup<sup>IVM-red</sup> mice, in which monocytes and neutrophils are fluorescently labelled (Fig. 1a–c and Extended Data Fig. 1h,i). Twenty-four hours after infection with 500 CFU *S. aureus* per bead, *Cx3cr1*-GFP<sup>+</sup> monocytes surrounded the infection site, whereas the majority of neutrophils infiltrated the infectious nidus (Fig. 1c,d). Quantification revealed that most monocytes (99.5%) were not in contact with *S. aureus* bacterial clusters (Fig. 1e,f); neutrophils were the main immune cell interacting with *S. aureus* (Fig. 1g). Flow cytometry analysis confirmed that neutrophils, rather than monocytes, had phagocytosed *S. aureus* (Extended Data Fig. 1j,k). Tracking cell behaviour over a period of 20 min revealed that monocytes were stationary, with barely detectable displacements (under 5  $\mu\text{m}$ ) and average velocity of  $0.56 \mu\text{m min}^{-1}$ , whereas neutrophils were dynamic at the infection site, with displacements of up to 20  $\mu\text{m}$  and an average velocity of  $2.35 \mu\text{m min}^{-1}$  (Extended Data Fig. 1l–m and Supplementary Video 1). These results suggest that at 24 h after infection, monocytes—unlike neutrophils—are not actively migrating in search of bacteria.

When we used a higher dose of  $10^7$  CFU per bead, we observed 80% fewer monocytes, whereas neutrophil recruitment was similar (Fig. 1c,d). Flow cytometry confirmed this dose-dependent immune response at 24 h after infection, with significantly more monocyte recruitment in the low-dose infection (Extended Data Fig. 2a,b). Despite the difference in the number of *Cx3cr1*-GFP<sup>+</sup> cells recruited (Extended Data Fig. 2b–d), the phenotypes of the cells were similar, with most being LY6C<sup>hi</sup> classical monocytes (Extended Data Fig. 2e,f). Monocyte recruitment was dependent on an active infection, as a bead coated with heat-killed *S. aureus* or a sterile bead did not elicit the same recruitment response at 24 h after treatment (Extended Data Fig. 2g,h).

## Monocyte recruitment and fate during infection

Over the course of 7 days, monocytes that were initially surrounding the infection at 24 h infiltrated into the infection site as monocytes (Fig. 1h–j) and became larger, resembling macrophage morphology by 7 days post-infection (Fig. 1k,l). Consistent with a transition to a macrophage phenotype, spinning-disk confocal intravital microscopy in *Cx3cr1<sup>GFP/+</sup>* *Ccr2<sup>RFP/+</sup>* mice revealed that once in the infectious milieu, these monocytes progressively down-regulated CCR2 expression between 24 h and 7 days post-infection (Extended Data Fig. 2i,j).

*Cx3cr1<sup>GFP/+</sup>* *Ccr2<sup>RFP/RFP</sup>* (CCR2-deficient) mice, which lack classical monocytes in the circulation were completely devoid of monocytes at the site of *S. aureus* skin infection, similar to *Cx3cr1<sup>GFP/+</sup>* *Ccr2<sup>RFP/+</sup>* mice treated with the anti-CCR2 antibody MC-21<sup>11</sup> (Fig. 1m,n), suggesting that the *Cx3cr1*-GFP<sup>+</sup> macrophages observed infiltrating the infection site at 7 days post-infection originated from classical monocytes. Flow cytometry analysis confirmed

that the CCR2-deficient mice were devoid of *Cx3cr1*-GFP<sup>+</sup>LY6C<sup>hi</sup> monocytes and *Cx3cr1*-GFP<sup>+</sup>LY6C<sup>low</sup> monocytes/macrophages at 24 h and 72 h post-infection, respectively (Extended Data Fig. 2k,l).

To evaluate the fate of early-recruited monocytes, we used a *Ccr2*-driven fate-mapping mouse, *Ccr2-creER<sup>T2</sup>;zGreen<sup>+/-</sup>*, in which *Ccr2*-expressing cells permanently turn on zGreen expression upon tamoxifen injection<sup>12,13</sup> (Extended Data Fig. 3a). CCR2-derived cells were observed at the site of infection at 24 h post-infection up to 14 days post-infection (Extended Data Fig. 3b). Flow cytometry analysis demonstrated that CCR2<sup>+</sup> monocytes (zGreen<sup>+</sup>LY6C<sup>hi</sup>CD64<sup>low/+</sup>) matured and differentiated into macrophages (zGreen<sup>+</sup>LY6C<sup>low</sup>CD64<sup>+/hi</sup>) over the course of infection (Extended Data Fig. 3c). These data show that during *S. aureus* skin infection, recruited CCR2<sup>+</sup> monocytes infiltrate the infection site, mature to monocyte-derived macrophage, and persist at the infection site to at least 14 days post-infection.

We next used spectral flow cytometry to profile monocyte/macrophage subtypes in wild-type and CCR2-deficient mice and observed a progressive maturation from P1 monocytes to P5 monocyte-derived tissue macrophages, as defined previously<sup>14</sup> (Extended Data Fig. 3d–f). There was a significant reduction in P1–P5 monocyte/macrophage subsets in CCR2-deficient mice (Extended Data Fig. 3f). CCR2 deficiency did not affect recruitment of other myeloid (neutrophils and LY6C<sup>+</sup>CD64<sup>+</sup>CD11b<sup>+</sup> dendritic cells) and non-myeloid cell types, including T cells, B cells, natural killer cells and LY6G<sup>+</sup>CD11b<sup>+</sup>CD3<sup>+</sup>CD19<sup>+</sup>B220<sup>+</sup>NK1.1<sup>+</sup> (Lin<sup>-</sup>) cells (Extended Data Fig. 3g).

## Monocytes are critical for repair post-infection

The observation that monocytes moved into the infection site before the full clearance of bacteria supported the notion that they may have an active role in bacterial clearance. However, we found that monocytes did not contribute to bacterial clearance in the skin, as there were no differences in skin bacterial burden between *Ccr2<sup>RFP/+</sup>* (wild-type) and *Ccr2<sup>RFP/RFP</sup>* (CCR2-deficient) mice at any time point between 1 and 30 days after infection, with complete eradication of *S. aureus* in both groups at 21 days (Fig. 2a). However, *S. aureus* clearance was dependent on neutrophils, as depletion of these cells led to a 100-fold increase in bacterial burden and massive abscess formation (Extended Data Fig. 4a–c). These data suggest that despite recruitment of large numbers of monocyte/macrophage cells in our model, these cells do not kill *S. aureus* in vivo, raising the possibility that monocytes have another function during bacterial clearance from skin.

To track the progression from infection to fully healed wound, we marked four quadrants of the skin with permanently tattooed spots<sup>15</sup> at the time of infection. These spots served as landmarks to identify the infected region, especially after resolution (Fig. 2b and Extended Data Fig. 5a–d). Although similar-sized wounds were present in both wild-type and CCR2-deficient mice at 14 days post-infection (Fig. 2c and Extended Data Fig. 5e), the wounds in CCR2-deficient mice were highly vascularized, with differences that were visible to the naked eye (Extended Data Fig. 5f). Using intravital microscopy, we imaged blood vessels at the infection site and found a significant overgrowth of the vasculature in CCR2-deficient wounds compared with wild-type wounds, including larger feeding arteries and much denser capillary networks (Fig. 2d and Supplementary Video 2). This could be measured as an increase in blood vessel volume at 14 days post-infection (Fig. 2e). Infection with *S. aureus* USA300 induced a similar increased vasculature response in CCR2-deficient mice (Fig. 2f). Monocyte depletion also increased vasculature at 14 days post-infection (Fig. 2g). Blood vessels in CCR2-deficient mice had increased permeability, indicating an immature, incompletely functional vasculature (Supplementary Video 2). This aberrant excessive vasculature was not observed in remote regions (a region of skin away from the infection in the same mouse, used here as an internal control) of both wild-type and CCR2-deficient mice (Extended Data Fig. 5g).

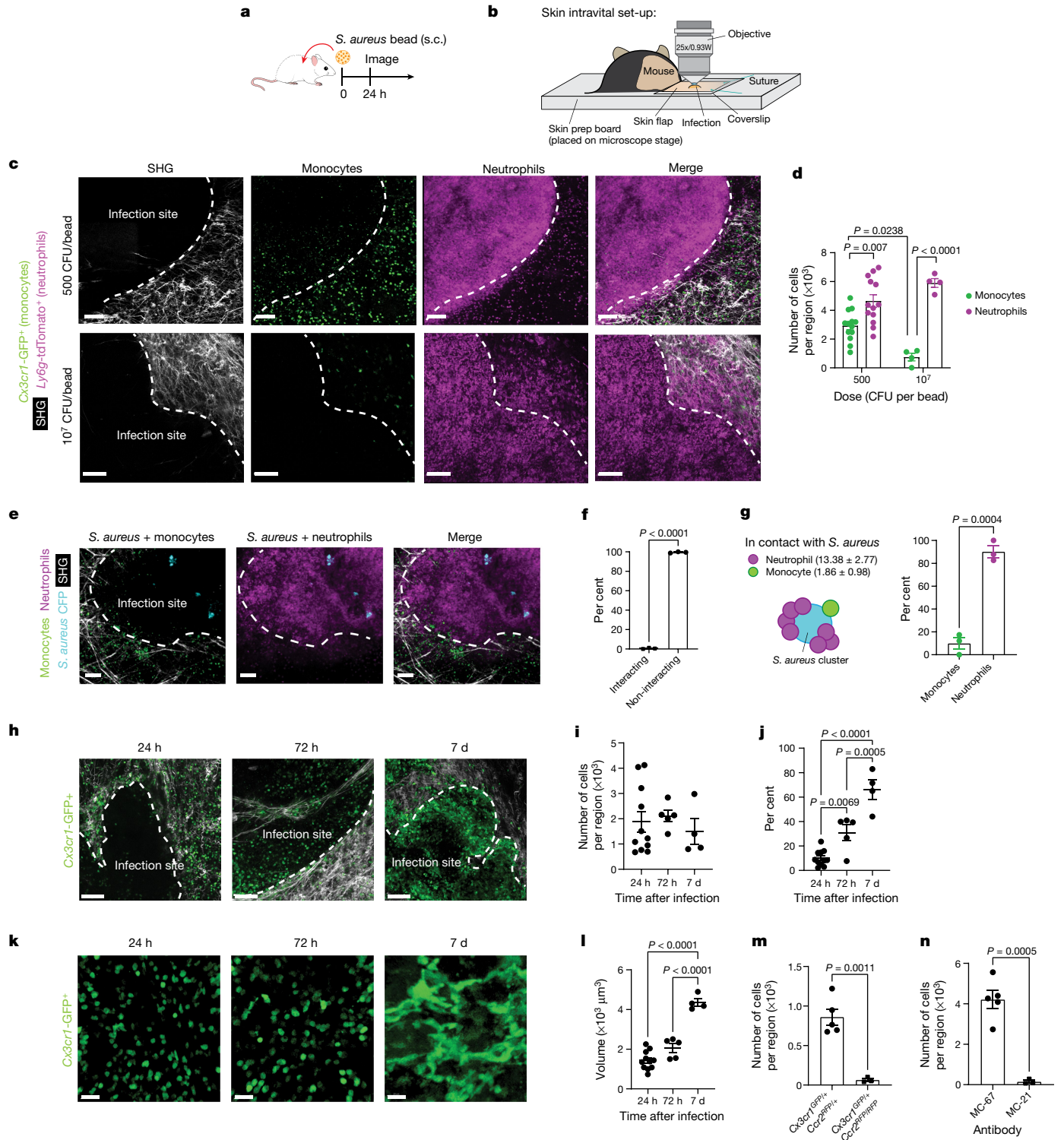


Fig. 1 | See next page for caption.

**Fig. 1 | Monocytes are recruited to low-dose *S. aureus* skin infection.**

**a**, Overview of the experimental subcutaneous (s.c.) model of infection. **b**, Schematic of the intravital imaging of mouse skin. **c,d**, *Cx3cr1*<sup>GFP/+</sup> Catchup<sup>IVM-red</sup> mice were infected with a low-dose (500 CFU per bead) or high-dose (10<sup>7</sup> CFU per bead) *S. aureus*-coated bead and imaged at 24 h post-infection by multiphoton intravital microscopy. **c**, Representative images of GFP<sup>+</sup> monocytes and tdTomato<sup>+</sup> neutrophils at the *S. aureus* bead. Dashed lines outline the infection site. Images are representative of *n* = 13 mice (low dose) and *n* = 4 mice (high dose) examined over 4 independent experiments. Scale bars, 100 μm. **d**, Numbers of GFP<sup>+</sup> monocytes and tdTomato<sup>+</sup> neutrophils per region. *n* = 13 mice for low dose and *n* = 4 mice for high dose examined over 4 independent experiments; data are mean ± s.e.m. Two-way ANOVA with Šidák's multiple comparisons test, *P* = 0.007 for low-dose monocytes vs neutrophils, *P* = 0.0238 for monocytes low dose vs high dose, *P* < 0.0001 for high-dose monocytes vs neutrophils, *P* = 0.4104 for neutrophils low dose vs high dose. **e–g**, *Cx3cr1*<sup>GFP/+</sup> Catchup<sup>IVM-red</sup> mice were infected with a low-dose bead coated with CFP-expressing *S. aureus* and imaged at 24 h post-infection. **e**, Representative image showing monocytes, neutrophils and CFP *S. aureus*. Dashed lines outline the infection site. Images representative of *n* = 3 mice examined over 2 independent experiments. Scale bars, 100 μm. **f**, Quantification of monocytes interacting with *S. aureus*. *n* = 3 mice examined over 2 independent experiments; data are mean ± s.e.m. Unpaired two-sided Student's *t*-test, *P* < 0.0001. **g**, Cartoon showing cells in contact with *S. aureus* (left) and the percentage of interacting cells (right). *n* = 3 mice examined over 2 independent experiments; data are mean ± s.e.m. Unpaired two-sided Student's *t*-test,

*P* = 0.0004. **h–i**, *Cx3cr1*<sup>GFP/+</sup> *Ccr2*<sup>RFP/+</sup> mice were infected with a low-dose *S. aureus* bead and imaged at 24 h, 72 h and 7 days post-infection. **h**, Representative images showing monocyte infiltration into the infection site. Dashed lines outline the infection site. Scale bars, 100 μm. Monocyte recruitment (**i**) and the percentage of monocytes infiltrating the infection (**j**). **k**, Representative images of monocyte morphology at 24 h, 72 h and 7 days post-infection. Scale bars, 20 μm. **l**, Monocyte volume. In **h,k**, images are representative of *n* = 11 mice (24 h), *n* = 5 mice (72 h), and *n* = 4 mice (7 days) per group examined over 3 independent experiments. In **i,j,l**, *n* = 11 mice (24 h), *n* = 5 mice (72 h), and *n* = 4 mice (7 days) per group examined over 3 independent experiments; data are mean ± s.e.m. One-way ANOVA with Tukey's multiple comparisons test. **i**, *P* = 0.9324 for 24 h vs 72 h, *P* = 0.8381 for 24 h vs 7 days, *P* = 0.7185 for 72 h vs 7 days. **j**, *P* < 0.0001 for 24 h vs 7 days, *P* = 0.0069 for 24 h vs 72 h, *P* = 0.0005 for 72 h vs 7 days. **l**, *P* < 0.0001 for 24 h vs 7 days and for 72 h vs 7 days, *P* = 0.0511 for 24 h vs 72 h. **m**, *Cx3cr1*<sup>GFP/+</sup> *Ccr2*<sup>RFP/+</sup> and *Cx3cr1*<sup>GFP/+</sup> *Ccr2*<sup>RFP/RFP</sup> mice were infected with a low-dose *S. aureus* bead, imaged at 24 h post-infection, and monocytes recruited to the infection were quantified. *n* = 5 mice (*Cx3cr1*<sup>GFP/+</sup> *Ccr2*<sup>RFP/+</sup>) and *n* = 3 mice (*Cx3cr1*<sup>GFP/+</sup> *Ccr2*<sup>RFP/RFP</sup>) per group examined over 2 independent experiments; data are mean ± s.e.m. Unpaired two-sided Student's *t*-test, *P* = 0.0011. **n**, *Cx3cr1*<sup>GFP/+</sup> *Ccr2*<sup>RFP/+</sup> mice treated with the monocyte-depleting antibody MC-21 or the isotype control antibody MC-67, infected with a low-dose *S. aureus* bead, and imaged at 24 h post-infection. Monocytes recruited to the infection were quantified. *n* = 5 mice (MC-67) and *n* = 3 mice (MC-21) per group examined over 2 independent experiments; data are mean ± s.e.m. Unpaired two-sided Student's *t*-test, *P* = 0.0005.

As a functional consequence, most wild-type mice were fully healed at 30 days post-infection, whereas wounds remained in CCR2-deficient mice (Fig. 2h,i and Extended Data Fig. 5h). Additionally, the wounds in CCR2-deficient mice had a thick collagenous capsule resembling a scar (Fig. 2j) and were still heavily vascularized at 30 days post-infection (Fig. 2k). Healed wounds in wild-type mice showed no such disruption to the collagen architecture (Fig. 2j). By 90 days post-infection, the wounds in most but not all CCR2-deficient mice were healed (Extended Data Fig. 5i–k). Finally, adoptive transfer of fluorescent CCR2-derived monocytes into CCR2-deficient hosts rescued the aberrant vasculature phenotype at 14 days post-infection (Fig. 2l–o), suggesting that recruited monocytes are critical for the resolution of infection by regulating angiogenesis and facilitating wound repair.

**Adipocyte expansion and leptin production**

To investigate the mechanism of dysregulated angiogenesis and delayed healing, we performed multiplexed enzyme-linked immunosorbent assay (ELISA) for repair mediators including growth factors and matrix metalloproteinases (MMPs) on skin wound homogenate from *Ccr2*<sup>RFP/+</sup> and *Ccr2*<sup>RFP/RFP</sup> mice at 7 and 14 days post-infection. There were no differences in the levels of MMP-2, MMP-3, MMP-8, MMP-12 or proMMP-9 (Extended Data Fig. 6a). From a panel of angiogenesis and growth factors, including angiopoietin-2, EGF, FGF-2, HGF, leptin, PLGF-2, SDF-1 and VEGF-A, only leptin differed between wild-type and CCR2-deficient mice at 14 days post-infection, with levels being higher in the wounds of CCR2-deficient mice (Fig. 3a and Extended Data Fig. 6b). Leptin levels were also increased in wounds from monocyte-depleted mice at 14 days post-infection (Fig. 3b). Leptin levels were similar in naive skin of wild-type and CCR2-deficient mice, but overall levels were more variable in the CCR2-deficient mice (Extended Data Fig. 6c). In addition, levels of pro-inflammatory and anti-inflammatory cytokines were not altered in CCR2-deficient mice (Extended Data Fig. 6d).

Adipocytes are the main producers of leptin. In response to *S. aureus* infection, hypodermal adipocytes expanded transiently in wild-type mice at 24 h post-infection, before resolving by 72 h (Extended Data Fig. 7a,b). By contrast, CCR2-deficient mice had a sustained hypodermal adipocyte expansion that persisted for 14 days (Fig. 3c,d). This

expansion was the result of adipocyte hypertrophy, as adipocytes from CCR2-deficient mice displayed an increase in size but not number compared with wild-type mice (Fig. 3e,f and Extended Data Fig. 7c). The hypodermal expansion was restricted to the infectious nidus, as distal regions of the skin at 24 h post-infection in either wild-type or CCR2-deficient mice were the same as in uninfected mice (Fig. 3c,d and Extended Data Fig. 7d). This localized expansion coincided with accumulation of BODIPY<sup>+</sup> adipocytes or lipid droplets within CCR2-deficient wounds (Extended Data Fig. 7e,f). Whole-mount staining at 14 days post-infection revealed that leptin expression was concentrated around adipocytes (LipidTOX<sup>+</sup>) within the wounds of CCR2-deficient mice (Extended Data Fig. 7g). This pericellular leptin distribution mirrored the perilipin-1 staining pattern of these adipocytes in skin cross-sections (Extended Data Fig. 7h). Finally, cytospin analysis of adipocytes isolated from the wounds of wild-type or CCR2-deficient mice confirmed that higher leptin protein expression in adipocytes from CCR2-deficient mice (Fig. 3g). These results suggest that there is an increased local leptin response in CCR2-deficient mice after infection, driven by expanded hypodermal adipocytes and adipocyte accumulation in the wounds.

**Leptin drives vascular overgrowth in infections**

Blocking leptin locally in CCR2-deficient mice with superactive mouse leptin antagonist (SMLA) reduced revascularization in the wounds (Fig. 4a–c), highlighting that this vascular response is driven by leptin. Furthermore, 50% of SMLA-treated CCR2-deficient mice showed no sign of a wound, whereas 100% of vehicle-treated mice still had a wound at 14 days post-infection (Fig. 4e). SMLA treatment of *Ccr2*<sup>RFP/+</sup> mice did not improve wound healing, vascular growth or decrease wound size (Extended Data Fig. 8a–d). To test whether leptin has a direct effect in stimulating angiogenesis, we administered recombinant leptin to wild-type mice and measured vascularity in the wounds at 14 days post-infection (Extended Data Fig. 8e–i). Treatment with exogenous leptin mimicked the CCR2-deficient phenotype at 14 days post-infection, with inappropriate hyper-vascularization (Extended Data Fig. 8f,g) but had no effect on the presence of wounds and no significant effect (*P* = 0.0571) on wound size at 14 days post-infection (Extended Data Fig. 8h,i). Leptin treatment of CCR2-deficient mice

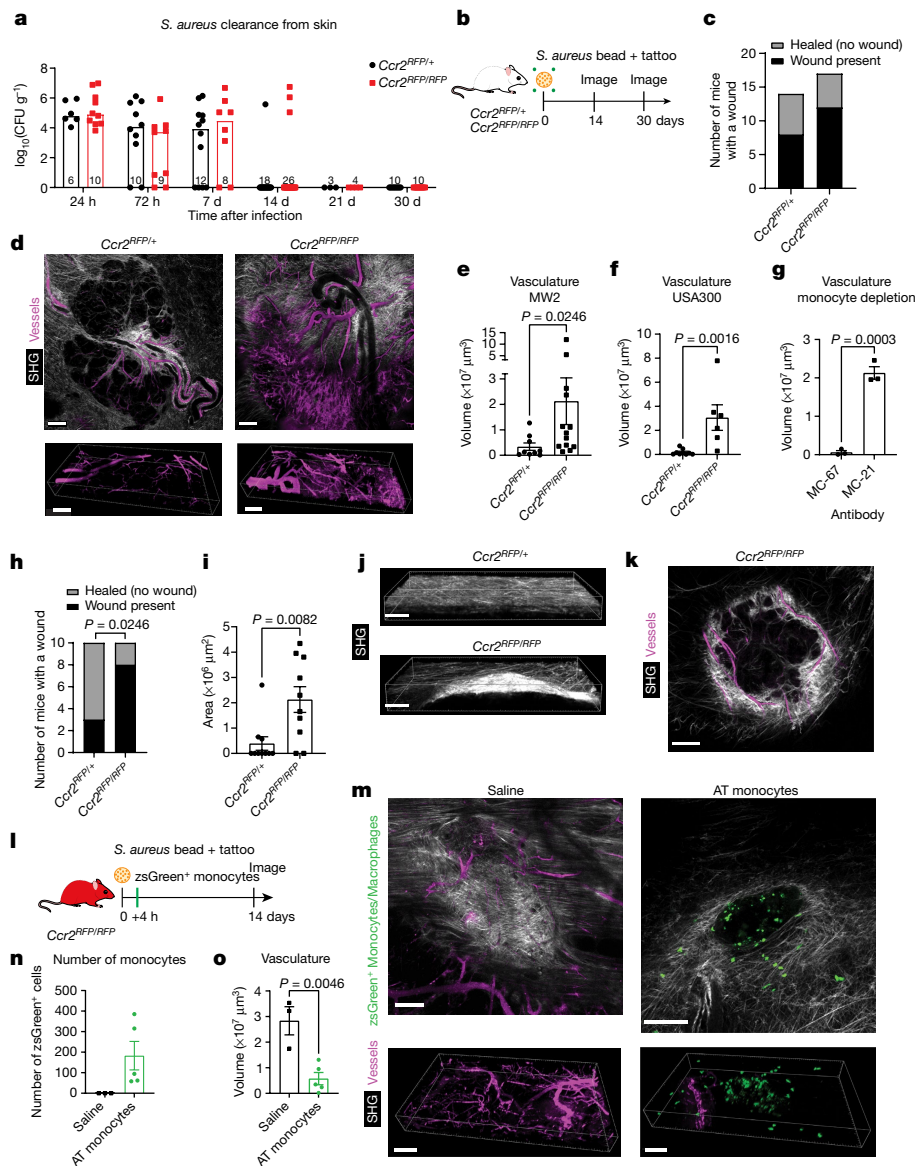


**Fig. 2 | Monocytes do not contribute to *S. aureus* clearance but are critical for tissue repair.** **a**, *Ccr2*<sup>RFP/+</sup> and *Ccr2*<sup>RFP/RFP</sup> mice were infected with a low-dose *S. aureus* bead and *S. aureus* in the skin was quantified at the indicated time points.  $n = 6$  (*Ccr2*<sup>RFP/+</sup> 24 h),  $n = 10$  (*Ccr2*<sup>RFP/+</sup> 72 h and 30 days),  $n = 12$  (*Ccr2*<sup>RFP/+</sup> 7 days),  $n = 18$  (*Ccr2*<sup>RFP/+</sup> 14 days),  $n = 3$  (*Ccr2*<sup>RFP/+</sup> 21 days),  $n = 9$  (*Ccr2*<sup>RFP/RFP</sup> 72 h),  $n = 8$  (*Ccr2*<sup>RFP/RFP</sup> 7 days),  $n = 26$  (*Ccr2*<sup>RFP/RFP</sup> 14 days), and  $n = 4$  (*Ccr2*<sup>RFP/RFP</sup> 21 days), from 8 independent experiments; data are median. Unpaired two-sided Student's *t*-test between individual time points,  $P = 0.6736$  for 24 h,  $P = 0.2915$  for 72 h,  $P = 0.5885$  for 7 days,  $P = 0.4801$  for 14 days. **b**, Experimental timeline for 14- and 30-day infections. **c–e**, *Ccr2*<sup>RFP/+</sup> and *Ccr2*<sup>RFP/RFP</sup> mice were infected with a low-dose *S. aureus* bead and imaged at 14 days post-infection. **c**, The presence of wounds in mice at 14 days post-infection.  $n = 14$  for *Ccr2*<sup>RFP/+</sup> and  $n = 17$  for *Ccr2*<sup>RFP/RFP</sup> mice examined over 6 independent experiments. Two-sided Chi-squared test,  $P = 0.4362$ . **d**, Representative images of vasculature in wounds. Top, 2D stitched image of an entire wound. Scale bar, 300  $\mu$ m. Bottom, 3D projection of vasculature. Scale bar, 200  $\mu$ m. Images are representative of  $n = 7$  for *Ccr2*<sup>RFP/+</sup> mice and  $n = 12$  for *Ccr2*<sup>RFP/RFP</sup> mice from 6 independent experiments. **e**, Vascular volume.  $n = 7$  for *Ccr2*<sup>RFP/+</sup> and  $n = 12$  for *Ccr2*<sup>RFP/RFP</sup> mice from 6 independent experiments; data are mean  $\pm$  s.e.m. Unpaired two-sided Mann-Whitney *U*-test,  $P = 0.0246$ . **f**, Vascular volume in wounds from *Ccr2*<sup>RFP/+</sup> and *Ccr2*<sup>RFP/RFP</sup> mice infected with a low-dose *S. aureus* USA300 bead at 14 days post-infection.  $n = 9$  for *Ccr2*<sup>RFP/+</sup> and  $n = 6$  for *Ccr2*<sup>RFP/RFP</sup> mice from 2 independent experiments; data are mean  $\pm$  s.e.m. Unpaired two-sided Mann-Whitney *U*-test,  $P = 0.0016$ . **g**, Vascular volume in wounds

from C57 mice treated with MC-67 or MC-21, infected with a low-dose *S. aureus* bead, and imaged at 14 days post-infection.  $n = 3$  per group from 2 independent experiments; data are mean  $\pm$  s.e.m. Unpaired two-sided Student's *t*-test,  $P = 0.0003$ . **h–k**, *Ccr2*<sup>RFP/+</sup> and *Ccr2*<sup>RFP/RFP</sup> mice were infected with a low-dose *S. aureus* bead and imaged at 30 days post-infection. The presence of wounds (**h**) and wound size (**i**).  $n = 10$  for *Ccr2*<sup>RFP/+</sup> and  $n = 10$  for *Ccr2*<sup>RFP/RFP</sup> mice from 2 independent experiments; data are mean  $\pm$  s.e.m. Two-sided Chi-squared test  $P = 0.0246$  (**h**); unpaired two-sided Mann-Whitney *U*-test,  $P = 0.0082$  (**i**). **j**, Representative image of skin collagen in *Ccr2*<sup>RFP/+</sup> and *Ccr2*<sup>RFP/RFP</sup> mice. Scale bar, 200  $\mu$ m. **k**, Representative image of a vascularized wound in a *Ccr2*<sup>RFP/RFP</sup> mouse. Scale bar, 200  $\mu$ m. **l–k**, Images are representative of  $n = 10$  mice for *Ccr2*<sup>RFP/+</sup> and  $n = 10$  mice for *Ccr2*<sup>RFP/RFP</sup>, from 2 independent experiments. **l–o**, *zsGreen*<sup>+</sup> monocytes were sorted from *Ccr2-creER*<sup>T2</sup>;*zsGreen*<sup>+/−</sup> mice and adoptively transferred into *Ccr2*<sup>RFP/RFP</sup> mice at 4 h post-infection with a low-dose *S. aureus* bead. **l**, Experimental timeline for adoptive transfer. **m**, Representative intravital images of *Ccr2*<sup>RFP/RFP</sup> mice after saline or adoptively transferred *zsGreen*<sup>+</sup> monocytes (AT monocytes) at 14 days post-infection. Top, 2D stitched image of wounds. Scale bar, 300  $\mu$ m. Bottom, 3D projection of vasculature. Scale bar, 200  $\mu$ m. Images are representative of  $n = 3$  mice (saline) and  $n = 5$  mice (AT monocytes) from 2 independent experiments. Monocyte numbers (**n**) and vascular volume (**o**) in wounds.  $n = 3$  mice (saline) and  $n = 5$  mice (AT monocytes) from 2 independent experiments; data are mean  $\pm$  s.e.m. (**n, o**). Unpaired two-sided Student's *t*-test,  $P = 0.0955$  (**n**); unpaired two-sided Mann-Whitney *U*-test,  $P = 0.0046$  (**o**).

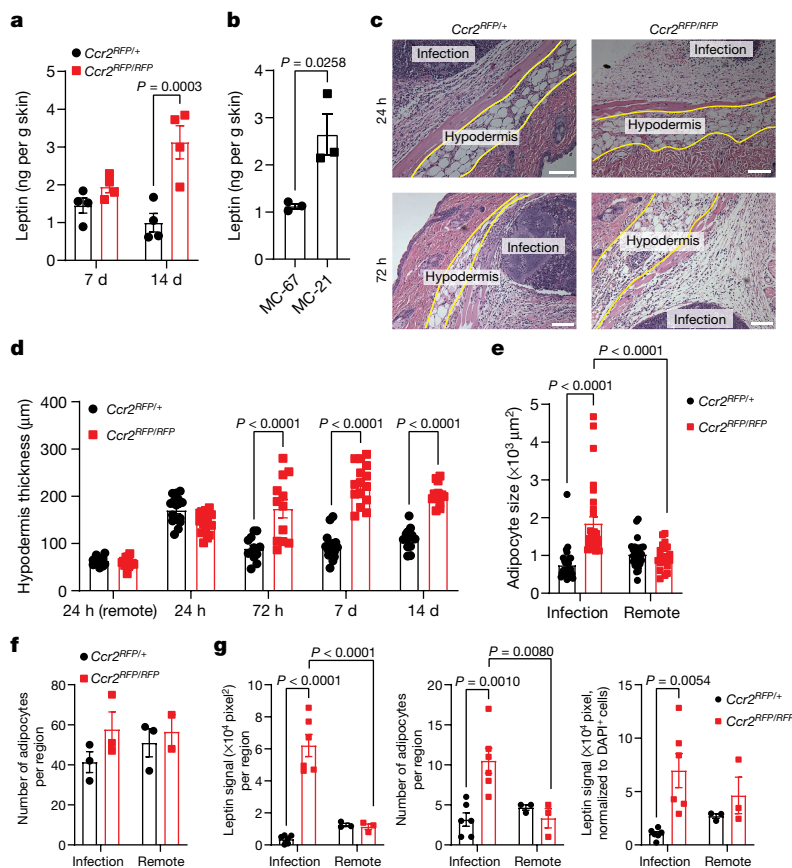


**Fig. 3 | Hypodermal expansion and elevated leptin in CCR2-deficient mice post-infection.** **a**,  $Ccr2^{RFP/+}$  and  $Ccr2^{RFP/RFP}$  mice were infected with a low-dose *S. aureus* bead, skin tissue was processed for ELISA at 7 and 14 days post-infection, and leptin levels were quantified.  $n = 4$  mice per group from 2 independent experiments; data are mean  $\pm$  s.e.m. Two-way ANOVA with Šidák's multiple comparisons test,  $P = 0.4191$  (7 days),  $P = 0.0003$  (14 days). **b**, C57 mice were treated with MC-67 or MC-21, infected with a low-dose *S. aureus* bead, skin tissue was processed for ELISA at 14 days post-infection, and leptin levels were quantified.  $n = 3$  mice per group from 2 independent experiments; data are mean  $\pm$  s.e.m. Unpaired two-sided Student's *t*-test,  $P = 0.0258$ . **c–f**,  $Ccr2^{RFP/+}$  and  $Ccr2^{RFP/RFP}$  mice were infected with a low-dose *S. aureus* bead and skin tissue was processed for haematoxylin and eosin (H&E) staining. **c**, Representative H&E images at 24 h and 72 h post-infection. The infection site and hypodermis are labelled. Scale bar, 100  $\mu$ m. Images are representative of  $n = 4$  mice (24 h) and 3 mice (72 h) from 2 independent experiments. Hypodermis thickness (**d**), adipocyte size (**e**) and number of adipocytes (**f**) at 24 h, 72 h, 7 days and 14 days post-infection. In **d, e**,  $n = 4$  mice (24 h and 7 days) and 3 mice (72 h and 14 days) per group from 2 independent experiments; 4 measurements per mouse (**d**);  $n = 30$  adipocytes ( $Ccr2^{RFP/+}$  ( $Ccr2$  wild-type) infection,  $Ccr2$  wild-type remote site and  $Ccr2^{RFP/RFP}$  infection) and  $n = 20$  adipocytes ( $Ccr2^{RFP/RFP}$  remote site) (**e**). In **f**,  $n = 3$  mice ( $Ccr2$  wild-type infection,  $Ccr2$  wild-type remote site and  $Ccr2^{RFP/RFP}$  infection) and  $n = 2$  mice ( $Ccr2^{RFP/RFP}$  remote site) per group from 2 independent experiments; data are mean  $\pm$  s.e.m. Mixed-effects model with Šidák's multiple comparisons test (**d–f**);  $P = 0.9990$  (24 h remote),  $P = 0.1063$

(24 h),  $P < 0.0001$  (72 h, 7 day and 14 day) (**d**);  $P = 0.9586$  ( $Ccr2^{RFP/+}$  remote vs  $Ccr2^{RFP/RFP}$  remote),  $P < 0.0001$  ( $Ccr2^{RFP/+}$  infection vs  $Ccr2^{RFP/RFP}$  infection),  $P = 0.0323$  ( $Ccr2^{RFP/+}$  infection vs  $Ccr2^{RFP/+}$  remote),  $P < 0.0001$  ( $Ccr2^{RFP/RFP}$  infection vs  $Ccr2^{RFP/RFP}$  remote) (**e**);  $P = 0.2747$  ( $Ccr2^{RFP/+}$  infection vs  $Ccr2^{RFP/RFP}$  infection),  $P = 0.8653$  ( $Ccr2^{RFP/+}$  remote vs  $Ccr2^{RFP/RFP}$  remote) (**f**). **g**,  $Ccr2^{RFP/+}$  and  $Ccr2^{RFP/RFP}$  mice were infected with a low-dose *S. aureus* bead and adipocytes were isolated for cytosin and leptin immunofluorescence. Leptin signal (left), total number of adipocytes (middle) and leptin signal normalized to number of DAPI<sup>+</sup> cells (right) among isolated adipocytes from wounds and from remote sites at 14 days post-infection on  $Ccr2^{RFP/+}$  and  $Ccr2^{RFP/RFP}$  mice.  $n = 6$  mice per group (infection) and 3 mice per group (remote site) from 2 independent experiments; each data point represents an average of 5 fields of view from one cytosin of one mouse; data are mean  $\pm$  s.e.m. Mixed-effects model with Šidák's multiple comparisons test. Leptin signal:  $P < 0.0001$  ( $Ccr2^{RFP/+}$  infection vs  $Ccr2^{RFP/RFP}$  infection),  $P = 0.2674$  ( $Ccr2^{RFP/+}$  remote vs  $Ccr2^{RFP/RFP}$  remote),  $P = 0.0047$  ( $Ccr2^{RFP/+}$  infection vs  $Ccr2^{RFP/+}$  remote),  $P < 0.0001$  ( $Ccr2^{RFP/RFP}$  infection vs  $Ccr2^{RFP/RFP}$  remote). Number of adipocytes:  $P = 0.0010$  ( $Ccr2^{RFP/+}$  infection vs  $Ccr2^{RFP/RFP}$  infection),  $P = 0.1979$  ( $Ccr2^{RFP/+}$  remote vs  $Ccr2^{RFP/RFP}$  remote),  $P = 0.3419$  ( $Ccr2^{RFP/+}$  infection vs  $Ccr2^{RFP/+}$  remote),  $P = 0.0080$  ( $Ccr2^{RFP/RFP}$  infection vs  $Ccr2^{RFP/RFP}$  remote). Normalized leptin signal:  $P = 0.0054$  ( $Ccr2^{RFP/+}$  infection vs  $Ccr2^{RFP/RFP}$  infection),  $P = 0.0887$  ( $Ccr2^{RFP/+}$  remote vs  $Ccr2^{RFP/RFP}$  remote),  $P = 0.3072$  ( $Ccr2^{RFP/+}$  infection vs  $Ccr2^{RFP/+}$  remote),  $P = 0.9855$  ( $Ccr2^{RFP/RFP}$  infection vs  $Ccr2^{RFP/RFP}$  remote).

did not result in a further increase in vasculature or wound phenotype (Extended Data Fig. 8j–m).

Leptin is an angiogenic factor, and has been shown to act directly on endothelial cells expressing the leptin receptor<sup>16,17</sup> (LEPR), suggesting a potential mechanism for the enhanced angiogenesis in CCR2-deficient mice. Single-cell RNA sequencing of P28 anagen back skin enriched in dermal fibroblasts, endothelial cells and pericytes with transgene reporter expression<sup>18</sup> revealed that arterial endothelial cells (*Pecam1<sup>+</sup>Fli1<sup>+</sup>*) express *Lepr* (Extended Data Fig. 9a–f). We confirmed that endothelial-specific leptin signalling stimulated vasculature in

monocyte-depleted mice by generating a *Lepr* conditional knockout in vascular endothelial cadherin<sup>+</sup> cells by crossing *Lepr<sup>f/f</sup>* mice to *Tg-Cdh5(PAC)-CreERT2* mice (Extended Data Fig. 9g–k).

On a systemic level, leptin levels are regulated by the counteracting hormone ghrelin<sup>19</sup>. We tested whether ghrelin could limit the vascular response to leptin, and whether exogenous ghrelin administration could rescue the aberrant vasculature detected in CCR2-deficient mice to the same extent as in SMLA-treated mice (Fig. 4a,b,d). Wound size was unaffected in ghrelin-treated CCR2-deficient mice (Extended Data Fig. 9l). Ghrelin treatment of wild-type mice improved wound

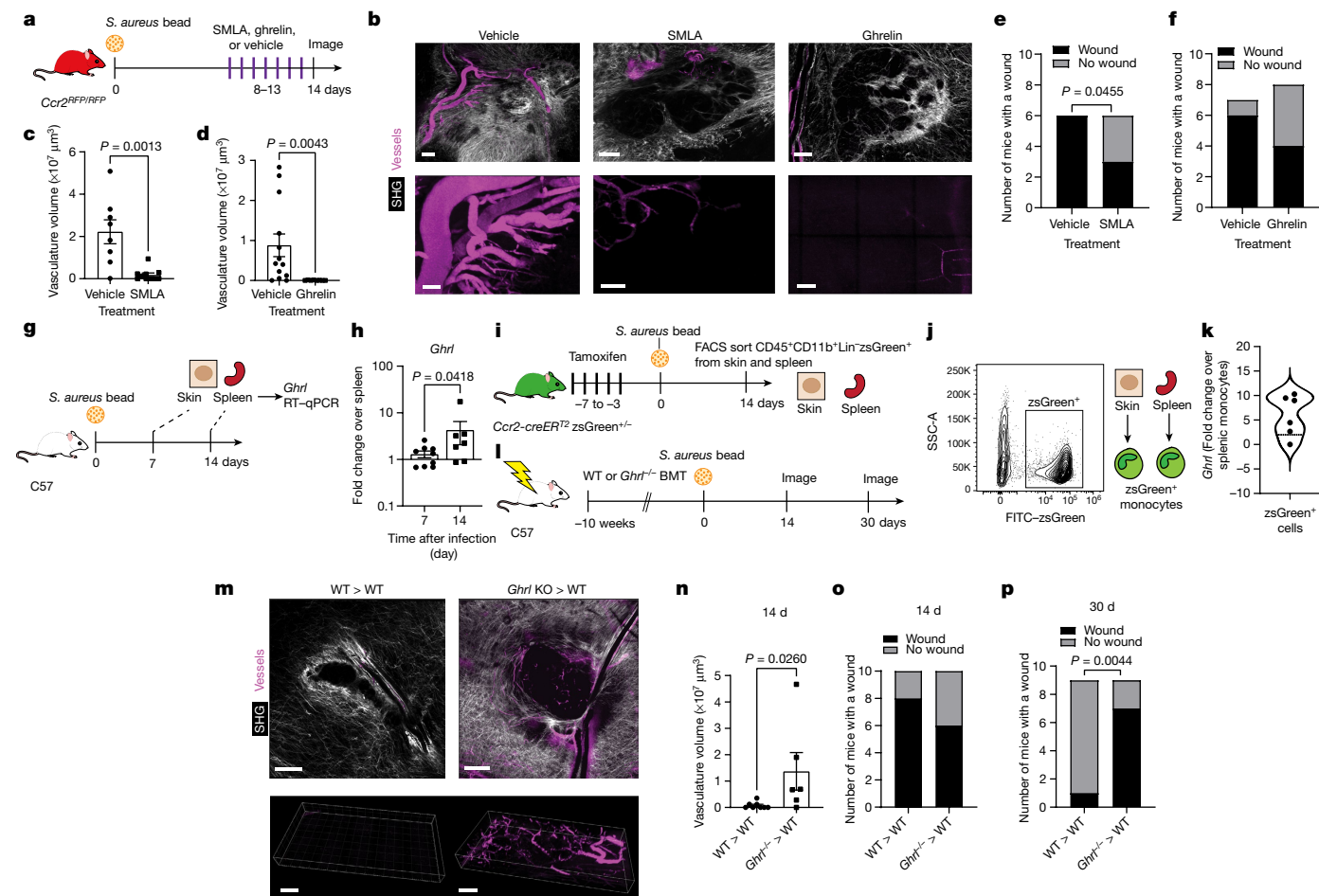


**Fig. 4 | Leptin drives dysregulated angiogenesis and delayed healing post-infection.** **a–f**, *Ccr2<sup>RFP/RFP</sup>* mice were infected with a low-dose *S. aureus* bead, treated with SMLA or ghrelin, and imaged at 14 days post-infection. **a**, Experimental timeline for SMLA and ghrelin treatment. **b**, Representative intravital image of vehicle-, SMLA- and ghrelin-treated infections in *Ccr2<sup>RFP/RFP</sup>* mice. Top, 2D stitched image of wound (scale bars, 300  $\mu$ m). Bottom, 3D projection of vasculature (scale bars, 100  $\mu$ m). Images are representative of  $n = 21$  mice (vehicle),  $n = 10$  mice (SMLA) and  $n = 8$  mice (ghrelin) from 4 independent experiments. **c**, Vascular volume in SMLA- and vehicle-treated *Ccr2<sup>RFP/RFP</sup>* mice.  $n = 8$  mice (vehicle) and  $n = 10$  mice (SMLA) per group from 2 independent experiments; data are mean  $\pm$  s.e.m. Unpaired two-sided Mann–Whitney *U*-test,  $P = 0.0013$ . **d**, Vascular volume in ghrelin- or vehicle-treated *Ccr2<sup>RFP/RFP</sup>* mice.  $n = 13$  mice (vehicle) and 8 mice (ghrelin) per group from 2 independent experiments; data are mean  $\pm$  s.e.m. Unpaired two-sided Mann–Whitney *U*-test,  $P = 0.0043$ . **e**, The presence of wounds in SMLA- and vehicle-treated *Ccr2<sup>RFP/RFP</sup>* mice.  $n = 6$  mice per group from 2 independent experiments. Two-sided Chi-squared test,  $P = 0.0455$ . **f**, The presence of wounds in ghrelin- or vehicle-treated *Ccr2<sup>RFP/RFP</sup>* mice at 14 days post-infection.  $n = 7$  mice (vehicle) and  $n = 8$  mice (ghrelin) per group from 2 independent experiments. Two-sided Chi-squared test,  $P = 0.1432$ . **g, h**, C57 mice were infected with a low-dose *S. aureus* bead and skin and spleen were processed for RNA isolation at 7 and 14 days post-infection. **g**, Experimental timeline for RNA isolation and quantitative PCR with reverse transcription (RT–qPCR). **h**, *Ghrl* mRNA expression in whole skin infections normalized to expression in spleen.  $n = 9$  mice (7 days post-infection) and 7 mice (14 days post-infection) per group

from 2 independent experiments; data are mean  $\pm$  s.e.m. Unpaired two-sided Mann–Whitney *U*-test,  $P = 0.0418$ . **i, k**, *Ccr2-creER<sup>2</sup>;zsGreen<sup>+/+</sup>* mice were treated with tamoxifen, infected with a low-dose *S. aureus* bead, and monocytes from 14 day post-infection skin and spleens were isolated for RNA isolation. **i**, Experimental timeline for isolation of zsGreen<sup>+</sup> monocytes from skin and spleen. **j**, Representative flow cytometry plot showing the gating strategy for isolation of zsGreen<sup>+</sup> monocytes. **k**, *Ghrl* expression in skin-derived monocytes shown normalized to expression in splenic monocytes.  $n = 6$  mice from 2 independent experiments. **l–p**, C57 mice were irradiated and bone marrow from wild-type (WT) or *Ghrl<sup>-/-</sup>* mice was adoptively transferred to the irradiated mice. Ten weeks later, mice were infected with a low-dose *S. aureus* bead and imaged at 14 or 30 days post-infection. **l**, Experimental timeline for bone marrow transfer and infection. **m**, Representative images of wounds in wild-type mice adoptively transferred with wild-type bone marrow (WT > WT) or *Ghrl<sup>-/-</sup>* bone marrow (*Ghrl<sup>-/-</sup>* > WT) at 14 days post-infection. Scale bars, 500  $\mu$ m (top) and 200  $\mu$ m (bottom). Images are representative of  $n = 8$  mice (WT > WT) and  $n = 6$  mice (*Ghrl<sup>-/-</sup>* > WT) from 2 independent experiments. **n**, Vasculature volume.  $n = 8$  mice (WT > WT) and  $n = 6$  mice (*Ghrl<sup>-/-</sup>* > WT) from 2 independent experiments; data are mean  $\pm$  s.e.m. Unpaired two-sided Mann–Whitney *U*-test,  $P = 0.0260$ . **o**, The presence of wounds at 14 days post-infection.  $n = 10$  mice per group from 2 independent experiments; two-sided Chi-squared test,  $P = 0.3291$ . **p**, The presence of wounds at 30 days post-infection.  $n = 9$  mice per group from 2 independent experiments. Two-sided Chi-squared test,  $P = 0.0044$ .

healing at 14 days post-infection (Extended Data Fig. 9m,n) but did not further reduce vasculature or wound size (Extended Data Fig. 9o,p).

We hypothesized that ghrelin may be produced locally by monocyte-derived cells to counteract leptin, thereby regulating

wound healing. We detected ghrelin mRNA in infected skin at 14 days post-infection (Fig. 4g,h). ZsGreen<sup>+</sup> monocyte-derived cells from 14-day infections in *Ccr2-creER<sup>2</sup>;zsGreen<sup>+/+</sup>* mice were positive for ghrelin transcript, suggesting that monocyte-derived ghrelin could contribute to leptin regulation (Fig. 4i–k).

Finally, wild-type mice reconstituted with ghrelin-deficient bone marrow had dysregulated vasculature at 14 days post-infection (Fig. 4l–o) and delayed healing at 30 days post-infection (Fig. 4p), whereas those reconstituted with wild-type bone marrow were normal, suggesting that hematopoietic-derived ghrelin is critical for regulating revascularization and wound healing. These results support the notion that leptin drives dysregulated angiogenesis and delayed healing response in CCR2-deficient mice, which can be counteracted by monocyte-derived ghrelin.

Our study identifies a mechanism for monocyte regulation of hypodermal adipocytes and associated leptin-mediated revascularization of wounds post-infection (Extended Data Fig. 10). We show that the functional role of monocytes during *S. aureus* skin infection is not to clear bacteria, but to facilitate proper tissue repair via maintenance of the hypodermal adipocyte layer and leptin levels. Mechanistically, we speculate that in addition to releasing ghrelin to oppose leptin function, monocytes may induce adipocyte lipolysis locally to prevent this response, as lipolysis has been shown to be critical for effective skin repair after sterile injury<sup>20</sup>. Adipocyte expansion ('reactive adipogenesis') during the early stages of *S. aureus* skin infection has been described<sup>21,22</sup>, but we show here that monocytes help regulate the contraction of this adipocyte layer, which is critical for proper healing. Monocytes have previously been shown to express ghrelin<sup>3,23</sup>, and we extend these observations to show that this is critical for regulation of subsequent wound repair and angiogenesis post-infection. In sterile skin wounds, leptin has been shown to mediate tissue repair through re-epithelialization<sup>24</sup>, but we find that excess leptin leads to locally dysregulated angiogenesis and a chronic wound. Once recruited to infected tissue, circulating monocytes must switch to a wound repair programme. Several studies suggest that tissue-resident macrophages—rather than circulating monocytes—contribute to repair<sup>25</sup>, but it is possible that the paucity of tissue-resident macrophages in the hypodermis makes the tissue more dependent on circulating monocytes. Moreover, the low infection burden enables monocytes to acquire a reparative programme. In sum, recruited monocytes are critical for the repair of skin following infection through local immune–adipokine crosstalk via ghrelin. This observation may also have implications for cancer and leptin-mediated angiogenesis in tumours<sup>26</sup> as well as other diseases.

## Online content

Any methods, additional references, Nature Research reporting summaries, source data, extended data, supplementary information, acknowledgements, peer review information; details of author contributions and competing interests; and statements of data and code availability are available at <https://doi.org/10.1038/s41586-022-05044-x>.

1. Shi, C. & Pamer, E. G. Monocyte recruitment during infection and inflammation. *Nat. Rev. Immunol.* **11**, 762–774 (2011).
2. Williams, M., Mildner, A. & Yona, S. Developmental and functional heterogeneity of monocytes. *Immunity* **49**, 595–613 (2018).
3. Dixit, V. D. et al. Ghrelin inhibits leptin- and activation-induced proinflammatory cytokine expression by human monocytes and T cells. *J. Clin. Invest.* **114**, 57–66 (2004).
4. Tsou, C. L. et al. Critical roles for CCR2 and MCP-3 in monocyte mobilization from bone marrow and recruitment to inflammatory sites. *J. Clin. Invest.* **117**, 902–909 (2007).
5. Cho, J. S. et al. Neutrophil-derived IL-1 $\beta$  is sufficient for abscess formation in immunity against *Staphylococcus aureus* in mice. *PLoS Pathog.* **8**, e1003047 (2012).
6. Feuerstein, R., Seidl, M., Prinz, M. & Henneke, P. MyD88 in macrophages is critical for abscess resolution in staphylococcal skin infection. *J. Immunol.* **194**, 2735–2745 (2015).
7. Brandt, S. L. et al. Macrophage-derived LT $\beta$  promotes abscess formation and clearance of *Staphylococcus aureus* skin infection in mice. *PLoS Pathog.* **14**, e1007244 (2018).
8. Thammavongsa, V., Missiakas, D. M. & Schneewind, O. *Staphylococcus aureus* degrades neutrophil extracellular traps to promote immune cell death. *Science* **342**, 863–866 (2013).
9. Willenborg, S. et al. CCR2 recruits an inflammatory macrophage subpopulation critical for angiogenesis in tissue repair. *Blood* **120**, 613–625 (2012).
10. Costerton, J. W., Stewart, P. S. & Greenberg, E. P. Bacterial biofilms: a common cause of persistent infections. *Science* **284**, 1318–1322 (1999).
11. Mack, M. et al. Expression and characterization of the chemokine receptors CCR2 and CCR5 in mice. *J. Immunol.* **166**, 4697–4704 (2001).
12. Croxford, A. L. et al. The cytokine GM-CSF drives the inflammatory signature of CCR2<sup>+</sup> monocytes and licenses autoimmunity. *Immunity* **43**, 502–514 (2015).
13. Carneiro, M. B. et al. Th1-Th2 cross-regulation controls early *Leishmania* infection in the skin by modulating the size of the permissive monocytic host cell reservoir. *Cell Host Microbe* **27**, 752–768.e757 (2020).
14. Tamoutounour, S. et al. Origins and functional specialization of macrophages and of conventional and monocyte-derived dendritic cells in mouse skin. *Immunity* **39**, 925–938 (2013).
15. Baranska, A. et al. Unveiling skin macrophage dynamics explains both tattoo persistence and strenuous removal. *J. Exp. Med.* **215**, 1115–1133 (2018).
16. Sierra-Honigsmann, M. R. O. et al. Biological Action of Leptin as an Angiogenic Factor. *Science* **281**, 1683–1686 (1998).
17. Bouloumié, A., Drexler, H. C., Lafontan, M. & Busse, R. Leptin, the product of *Ob* gene, promotes angiogenesis. *Circ. Res.* **83**, 1059–1066 (1998).
18. Abbasi, S. et al. Distinct regulatory programs control the latent regenerative potential of dermal fibroblasts during wound healing. *Cell Stem Cell* **27**, 396–412.e396 (2020).
19. Klok, M. D., Jakobsdottir, S. & Drent, M. L. The role of leptin and ghrelin in the regulation of food intake and body weight in humans: a review. *Obes. Rev.* **8**, 21–34 (2007).
20. Shook, B. A. et al. Dermal adipocyte lipolysis and myofibroblast conversion are required for efficient skin repair. *Cell Stem Cell* **26**, 880–895.e886 (2020).
21. Zhang, L. J. et al. Dermal adipocytes protect against invasive *Staphylococcus aureus* skin infection. *Science* **347**, 67–71 (2015).
22. Dokoshi, T. et al. Hyaluronidase inhibits reactive adipogenesis and inflammation of colon and skin. *JCI Insight* **3**, e123072 (2018).
23. Seim, I., Crisp, G., Shah, E. T., Jeffery, P. L. & Chopin, L. K. Abundant ghrelin gene expression by monocytes: putative implications for fat accumulation and obesity. *Obes. Med.* <https://doi.org/10.1016/j.obmed.2016.12.001> (2017).
24. Frank, S., Stallmeyer, B., Kämpfer, H., Kolb, N. & Pfeilschifter, J. Leptin enhances wound re-epithelialization and constitutes a direct function of leptin in skin repair. *J. Clin. Invest.* **106**, 501–509 (2000).
25. Wynn, T. A. & Vannella, K. M. Macrophages in tissue repair, regeneration, and fibrosis. *Immunity* **44**, 450–462 (2016).
26. Gonzalez-Perez, R. R., Lanier, V. & Newman, G. Leptin's pro-angiogenic signature in breast cancer. *Cancers* **5**, 1140–1162 (2013).

**Publisher's note** Springer Nature remains neutral with regard to jurisdictional claims in published maps and institutional affiliations.

© Crown 2022

## Methods

### Mice

Animal experiments were performed with adult male and female 7- to 8-week-old mice and all experimental animal protocols were approved by the University of Calgary Animal Care Committee and followed guidelines established by the Canadian Council for Animal Care (protocol number AC19-0138). All mice were housed under a 12 h:12 h light:dark cycle at 22–25 °C and 30–70% humidity under specific pathogen-free conditions. Mice received sterilized rodent chow and water ad libitum. Mice infected longer than 24 h were stored in a biohazard facility biosafety level 2. C56BL/6, *Cx3cr1<sup>GFP/+</sup>*, and *Cx3cr1<sup>GFP/GFP</sup>* mice were purchased from The Jackson Laboratory and bred in house. *Ly6G-cre/Ai14* (Catchup<sup>IVM-red</sup>) mice were a gift from M. Gunzer. We crossed Catchup<sup>IVM-red</sup> mice to *Cx3cr1<sup>GFP/GFP</sup>* mice to generate *Cx3cr1<sup>GFP/+</sup>* Catchup<sup>IVM-red</sup> double-reporter mice. Generation of *Ccr2<sup>RFP/RFP</sup>* (CCR2-deficient) and *Ccr2<sup>RFP/+</sup>* (CCR2-knock-in) mice have been previously described<sup>27</sup>. *Cx3cr1<sup>GFP/+</sup>* *Ccr2<sup>RFP/+</sup>* mice were generated by crossing *Cx3cr1<sup>GFP/GFP</sup>* *Ccr2<sup>RFP/RFP</sup>* mice with C57BL/6 mice. *Ccr2-creER<sup>T2</sup>;zsGreen<sup>+/-</sup>* mice were a gift from N. Peters and were made by B. Becher. Wild-type and *Ghrl<sup>-/-</sup>* bones were provided by Y. Sun for bone marrow transfers into C57 mice. *Lepr<sup>fl/fl</sup>* mice were a gift from T. Kieffer. *Cdh5(PAC)-CreER<sup>T2</sup>* mice were from Taconic. We crossed the *Lepr<sup>fl/fl</sup>* mice with the *Cdh5(PAC)-CreER<sup>T2</sup>* mice to generate *Lepr<sup>fl/fl</sup>* *Cdh5(PAC)-CreER<sup>T2</sup>* mice and *Lepr<sup>fl/fl</sup>* littermate controls.

### Bacterial strains

*S. aureus* strain USA400 MW2<sup>28</sup> was used for all experiments except for one experiment in which we used *S. aureus* USA300 LAC<sup>29</sup>. Both strains were a gift from M. Otto. Bacteria were grown in brain heart infusion (BHI) medium at 37 °C with shaking. When required, MW2 was transformed with pCM29 to constitutively express GFP or CFP<sup>30</sup>. For MW2-GFP and MW2-CFP growth, chloramphenicol (10 µg ml<sup>-1</sup>) was added for plasmid selection. For infection, *S. aureus* strains were sub-cultured in BHI medium without antibiotics until late exponential phase ( $A_{660} = 1.5$ ), washed once with sterile PBS, and resuspended in 1 ml PBS for bead or planktonic infections.

### *S. aureus* agar bead preparation

*S. aureus*-coated agar beads were used to model a foreign body infection, as previously described<sup>31</sup>. For beads with 10<sup>7</sup> CFU *S. aureus* per bead, no serial dilution was made. For beads with 500 CFU *S. aureus* per bead, bacteria were resuspended in 1 ml PBS, adjusted to an  $A_{660}$  of 0.100, then diluted tenfold. Two-hundred and fifty microlitres of bacterial suspension was then added to 2.25 ml of freshly autoclaved, warm, liquid 1.5% BHI agar. The agar–bacteria mixture was slowly dropped into 40 ml ice-cold mineral oil solution containing 400 µl Tween-20 to prevent bead clumping. Gentle stirring for 15 min in an ice bath yielded spherical *S. aureus* agar beads. The beads were washed with sterile PBS by spinning in a centrifuge at 2,000 rpm for 10 min. This wash step was repeated up to eight times to remove the mineral oil coating the beads. Beads were stored at 4 °C for up to 2 days, and fresh beads were made before every experiment. Validation of *S. aureus* bead concentrations of every bead batch were confirmed by mechanical disruption three times with an insulin syringe in 1 ml sterile PBS. Fifty microlitres of the bead solution was plated onto BHI agar plates and grown overnight at 37 °C to count bacterial titres. An average of four beads was used to determine the titre for each batch of beads.

### *S. aureus* bead infection model

Mice were anaesthetized with isoflurane gas, back hair was shaved, and hair was chemically removed with Nair hair removal cream. Nair cream was washed off with water and skin was dried with a gauze pad. Mice were tattooed with green animal tattoo ink to permanently mark the infection site. A single bead was picked up with forceps and placed

onto the bore of a needle connected to a syringe containing 50 µl sterile PBS, and the bead was moved back with a gentle pull of the syringe, which moved the bead into the needle tip. The bead was injected subcutaneously into the dorsal flank skin within the tattooed region. After injection, the agar bead degrades over 14 days which allows for proper wound healing in wild-type mice.

### Planktonic *S. aureus* infection model

For planktonic infections, bacteria from sub-cultures were diluted to 10<sup>4</sup> CFU ml<sup>-1</sup> in sterile PBS and mice were injected with 50 µl of bacteria, receiving approximately 500 CFU *S. aureus*. Bacteria from the 10<sup>4</sup> CFU ml<sup>-1</sup> stock were plated on BHI agar plates at 37 °C overnight to confirm bacterial inoculum.

### Antibodies and reagents

Antibodies used for flow cytometry were purchased from eBioscience, BioLegend or BD Biosciences. Dead cells were excluded by a fixable viability dye (Ghost Red 710, Tonbo Biosciences). All antibodies used in this study are listed in Supplementary Table 1. qTracker655 vascular label (ThermoFisher) was used to label blood vasculature. Recombinant mouse leptin was purchased from Sigma. Super Mouse Leptin Antagonist (SLAN-1 GENE ID 16846) was purchased from Protein Laboratories Rehovot Ltd. Recombinant mouse ghrelin (GS-*S(n-octanoyl)*-FLSP-EHQKAQRKESKPPAKLQPR) was purchased from Anaspec. LipidTOX Green and Red (ThermoFisher) was used to image adipocytes and lipid droplets.

### Skin imaging

Mice were placed under anaesthetic (ketamine (200 mg kg<sup>-1</sup>) and xylazine (10 mg kg<sup>-1</sup>) by intraperitoneal injection) and a jugular catheter was inserted as previously described<sup>32</sup>. Anaesthetics were administered through an intravenous catheter at regular intervals to keep the mouse sedated. The skin surgical procedure was performed as previously described<sup>33</sup>. In brief, mice were placed on a heating pad (World Precision Instruments) maintained at 37 °C. A midline incision was made on the dorsal side of the mouse and the flank skin was exposed and secured using silk sutures onto a skin prep board (3D-printed in house). A superfusion system was set up with Hank's balanced salt solution (HBSS) heated to 37 °C to perfuse the exposed skin tissue at a flow rate of 0.05. A cover glass was placed on top of the exposed skin for imaging.

### Resonant scanning multiphoton intravital microscopy

Intravital image acquisition of the skin was performed with an upright Leica SP8 resonant scanning multiphoton microscope equipped with a 20× 0.95 NA water objective. LasX software (v3.5.7.23225) was used for image acquisition. A tunable multiphoton laser was set to 940 nm for excitation of GFP, tdTomato and qTracker655 for blood vessels. Second harmonic generation was visualized at an emission of 470 nm. External hybrid detectors were used to detect emission at 620–680 nm (HyD-RLD1), 565–620 nm (HyD-RLD2), 495–565 nm (HyD-RLD3) and <495 nm (HyD-RLD4). For 3D time-lapse videos, three fields of view were selected within the infection area at 50 µm z-stack with 5 µm z-step size. Intervals were set to 30.0 s and videos were acquired over 20 min. After videos were acquired, two-three 3D regions were imaged to capture the infection area at the following dimensions: 2 × 5 tile scan at 200 µm z-stack with 5 µm z-step size. All videos and images used a line averaging of 16.

### Image processing, analysis and quantification

Raw imaging data was processed and quantified using Imaris Bitplane version 9.5. A Gaussian filter and background subtraction was applied to all images. A MATLAB XTension 'Channel Arithmetics' was run to subtract autofluorescent cells from vasculature (Ch1[vasculature] – Ch 2[autofluorescence]) (MATLAB version R2022a). 3D surface models of collagen and blood vasculature were generated in Imaris using default

parameters for collagen and a manual intensity threshold for blood vasculature. Imaris spot function was used for automated cell counting using default parameters, and then all spots were filtered by volume to exclude spots  $<5 \mu\text{m}^3$ . For quantification of monocyte infiltration, a  $25 \mu\text{m}$  z-stack was cropped at the focal plane of the infection site, a mask was applied to the collagen surface, then an intensity max filter was applied to the *Cx3cr1*-GFP<sup>+</sup> spots to define spots as collagen mask<sup>+</sup> or collagen mask<sup>-</sup>. For quantification of immune cell track length and velocity, tdTomato<sup>+</sup> and *Cx3cr1*-GFP<sup>+</sup> spots were tracked with Brownian motion over the 20 min video and xyz coordinates were exported to Rstudio, where the data was quantified using an Rscript for generation of the spider plots and velocity measurements. For quantification of monocyte hues, monocyte spots were manually counted in ImageJ using the multi-point selection tool and total counts of each colour were exported for quantification. For monocyte and neutrophil distance to *S. aureus* clusters, surfaces were defined on the clusters of CFP-expressing *S. aureus* and spots for monocytes and neutrophils. Interacting cells were defined as spots within one cell body ( $<7 \mu\text{m}$ ) from a *S. aureus* surface.

### Bacterial cell counting

Skin infections (1 cm<sup>2</sup> biopsy) and peripheral organs were collected at different time points, homogenized in PBS and serial dilutions were plated on BHI agar plates and colonies were counted after 18 h at 37 °C. For blood titres, blood was collected via cardiac puncture and put into a heparinized collection tube, serial dilutions were plated on BHI agar plates and colonies were counted after 18 h at 37 °C.

### Measurement of growth factors, MMP and cytokine concentrations

A multiplex ELISA was performed to quantify levels of angiogenic factors, growth factors and MMPs within the skin tissue homogenate. After imaging, skin wounds were collected into PBS containing protease inhibitor cocktail tablet (Sigma Aldrich) and homogenised. Skin homogenate was spun down for 10 min at 3,000 rpm and the supernatant was stored at -20 °C for multiplex ELISA. ELISA was performed as per company protocol (Eve Technologies). For measurement of leptin concentrations after monocyte depletion, a leptin ELISA kit (Abcam) was used according to the manufacturer's instructions.

### Flow cytometry

Skin biopsies of the infected area were collected (1 cm<sup>2</sup> section) and collected into cold HBSS. Skin tissue was digested as previously described<sup>34</sup>. Skin tissue was incubated at 37 °C with gentle rotation for 75 min in 2 ml of HBSS containing 3% FBS, 5 mM EDTA and 0.8 mg ml<sup>-1</sup> collagenase II (Worthington). Following enzymatic digestion, tissue was passed through a 70- $\mu\text{m}$  filter and washed with HBSS containing 3% FBS and 5 mM EDTA. A debris-removal step was performed as per manufacturer protocol in the debris-removal kit (Miltenyi Biotec). Single cells were resuspended in 800  $\mu\text{l}$  of HBSS containing 3% FBS and 5 mM EDTA and 200  $\mu\text{l}$  was used for antibody staining. Blood was obtained by intra-cardiac bleed and red blood cells were lysed with ACK lysing buffer. Antibody staining of surface-expressed molecules were performed as described. Cells were first stained with Fc blocking antibody (1:200) and Ghost Red 710 fixable viability dye (1:6,400) in HBSS for 30 min on ice. CCR2 antibody staining was done at 37 °C for 20 min. Next, cell suspensions were stained for remaining surface antigens in HBSS supplemented with 3% FBS and 5 mM EDTA for 20 min on ice. When indicated, *Cx3cr1*<sup>GFP/+</sup> *Ccr2*<sup>REP/+</sup> transgenic reporter mice were used for identifying monocyte subsets using flow cytometry. After washing with HBSS containing 3% FBS and 5 mM EDTA, cells were fixed with 1% paraformaldehyde in HBSS for 15 min on ice and then run the following day on the Cytotex flow cytometer with software SpectroFlow (v3.0.3, 11292021) or Cytek spectral cytometer with software

CytExpert (v2.4). All flow cytometry experiments were analysed with FlowJo v10 (Tree Star).

### In vivo antibody treatment and depletion studies

Neutrophil depletion was performed by intraperitoneal administration of 200  $\mu\text{g}$  of anti-LY6G antibody (1A8 clone, Bio X Cell) 24 h prior to infection and every 24 h thereafter. 200  $\mu\text{g}$  of isotype antibody (2A3 clone, Bio X Cell) was used as control treatment. Monocyte depletion was performed by intravenous administration of 20  $\mu\text{g}$  of MC-21 at the time of infection ( $t = 0$ ) and every 24 h thereafter for 5 consecutive doses<sup>11</sup>. Twenty micrograms of isotype antibody (MC-67) was used as control treatment.

### Tamoxifen treatment and fate-mapping studies

We used a recently acquired *Ccr2-creER*<sup>T2</sup> mouse<sup>12</sup> crossed with Ai6(RCL-zsGreen1) mice in which *Ccr2*-expressing cells permanently turn on zsGreen expression following treatment with tamoxifen. Tamoxifen treatment was performed daily on days -7 to -3 before infection at day 0. Mice received intraperitoneally 200 mg kg<sup>-1</sup> body weight of tamoxifen dissolved in sterile corn oil. zsGreen<sup>+</sup> cells were tracked via flow cytometry and by multiphoton intravital microscopy (MP-IVM).

### Adoptive transfer of monocytes

Spleen, blood and bone marrow was collected from tamoxifen-treated *Ccr2-creER*<sup>T2</sup> mice. Single cells were isolated from each organ and monocytes were enriched using a MACS Miltenyi Biotec monocyte isolation kit as per manufacturer's protocol. Enriched monocytes from spleen, blood and bone marrow were pooled together from 8 mice and then zsGreen<sup>+</sup> monocytes were sorted using FACS. Approximately 300,000 monocytes were adoptively transferred i.v. into CCR2-deficient mice at 4 h post-infection and mice were imaged at 14 days post-infection.

### Leptin, SMLA and ghrelin treatment

Mice were treated subcutaneously with recombinant leptin (3.0 mg kg<sup>-1</sup>) on days 8, 10 and 12 post-infection. For SMLA (1.5 mg kg<sup>-1</sup>) or recombinant ghrelin (1.5 mg kg<sup>-1</sup>) treatment, mice were treated subcutaneously daily on days 8–13 post-infection. Mice were injected with an equivalent volume of saline as vehicle treatment. Mice were then imaged at 14 days post-infection and vasculature was measured inside the wounds.

### Adipocyte isolation and cytopins

Adipocytes were isolated from the skin as previously described with the following modifications<sup>34</sup>. In brief, skin infections were digested in 0.8 mg ml<sup>-1</sup> collagenase type II (Worthington Biochemical, LS004174) in HBSS containing 3% BSA, for 75 min at 37 °C with gentle shaking. Samples were shaken vigorously by hand for 1 min after 1 h of digestion. The digested suspension was filtered through a 250- $\mu\text{m}$  nylon filter and centrifuged at 300g for 3 min, after which floating adipocytes and supernatant were removed using a sterile plastic transfer pipette. Adipocytes were washed in HBSS containing 3% BSA and 100  $\mu\text{l}$  of the floating adipocyte suspension was used for cytopins and immunofluorescence staining. All immunofluorescence staining procedures were done at room temperature in the dark. In preliminary experiments it was verified that adipocytes on cytopins were viable prior to fixation and staining using a zombie green fixable viability dye. Cytopin slides of adipocytes were fixed with 3% paraformaldehyde for 10 min, permeabilized with HBSS containing 0.1% saponin for 30 min, then incubated in blocking solution containing 10% normal goat serum in HBSS for 30 min. Adipocytes were then incubated with primary antibody rabbit anti-leptin (1:100) in blocking solution for 1 h, washed with blocking solution, then incubated with goat anti-rabbit secondary IgG for 1 h. Adipocytes were washed with PBS and then stained with LipidTOX (1:200 in PBS) and CellMask orange (1:1,000 in PBS) for 30 min. Slides were mounted with two drops of Mounting Medium with DAPI-Aqueous,

# Article

Fluoroshield (Abcam) and sealed with a coverslip. Images were acquired using an upright Leica SP8 resonant scanning confocal microscope.

## Histology

Skin infections were collected and fixed in 4% paraformaldehyde for 48 h at 4 °C, then transferred to PBS. A surgical blade was used to cut the infection in half in line with hair follicle growth, and skin tissue was either embedded in OCT for cryosectioning (Leica Biosystems) at 50 µm slices for immunofluorescence staining, or embedded in paraffin and cut at 5 µm slices for H&E staining. H&E images were acquired on an Olympus IX51 Histology Microscope using software Olympus cellSens Standard 1.18 (Build 16686). Hypodermal thickness was analysed manually using ImageJ (NIH). In brief, the line tool was applied to measure the thickness of the hypodermis defined as from the end of the dermis to the start of the panniculus carnosus muscle. Four line measurements from two fields of view per mouse (20× magnification) were used for quantification.

## Immunofluorescence

To obtain tissue for cryostat sections from *Ccr2<sup>RFP/+</sup>* and *Ccr2<sup>RFP/RFP</sup>* mice, skin wound sites were dissected and fixed in 4% paraformaldehyde for 24 h at 4 °C. After rinsing with PBS (3 × 10 min), tissues were incubated in 20% sucrose in PBS for 24 h at 4 °C to cryoprotect them. They were then embedded in Clear Frozen Section compound (VWR) and frozen on dry ice. Cryostat sections were cut at 20 µm and collected on adhesive coated glass slides, with adjacent sections on consecutive slides. Cryostat sections were equilibrated to room temperature, washed in PBS containing 0.1% Triton X-100 (3 × 10 min; Sigma Aldrich) and blocked in 5% donkey serum, 1% BSA and 0.4% Triton X-100 diluted in PBS for 2 h at room temperature. A rabbit polyclonal antibody for leptin (1:50; Abcam, ab16227) was applied to sections on one slide and a rabbit polyclonal antibody for perilipin-1 (1:500; Abcam, ab3526) was applied to adjacent sections on another slide and incubated for 72 h at 4 °C. It was necessary to stain adjacent sections (20 mm apart) due to the inability to double label with both antibodies since both were raised in rabbit. Sections were washed with PBS (3 × 10 min) and incubated in donkey anti-rabbit secondary antibody conjugated to Alexa Fluor 488 or goat anti-rabbit CY5 (1:100; Jackson Immuno-research Labs) for 1–2 h at room temperature. Tissues were washed in PBS (3 × 10 min) and mounted with bicarbonate-buffered glycerol and stored under dark conditions at 4 °C. Sections were stained without a primary antibody to serve as a control for the secondary antibody labelling. Tissues were viewed using a Zeiss Axioplan fluorescence microscope (Zeiss) and images captured with a Moment CMOS digital monochrome camera (Teledyne Photometrics). Since all tissues were RFP-positive, double-labelled images with the RFP label were obtained for both leptin and perilipin-1. For immunostaining of adipocytes and lipid droplets, slides were stained with BODIPY (1:1,000, Sigma; 1:1,000, D3922, Invitrogen) and nuclei were labelled with DAPI (1:500; Sigma). Images were captured using a Leica SP8 spectral confocal microscope. Z-stacks of all images were projected into a single image and the full drop was digitally reconstructed by stitching the different image projections using the Leica Software. Images are tiled and stitched with LasX software (v3.5.5.19976).

## Whole-mount 3D confocal microscopy

Skin samples were collected from mice and fixed in 4% PFA for 48 h at 4 °C. Samples were then washed 3 times in 1% PBS for 1 h at 4 °C, shaking and left in 1% BSA 1% Triton X-100 PBS overnight in 4%, shaking. Tissues were then stained with rabbit anti-leptin antibody (Abcam, 1:200 dilution) in 1% Triton X-100 and 1% BSA PBS for 3 days 4 °C, shaking. Next, the samples were washed and stained with secondary antibodies (1:200) for 2 days 4 °C, shaking. Samples were then washed and stained for 30 min with LipidTOX (1:500) at room temperature. Finally, the tissues were washed and mounted onto a glass coverslip and imaged using an

Olympus IX81 inverted microscope and Volocity image acquisition software (v6.1.1).

## Scanning electron microscopy

Skin infections were collected and immediately fixed in a solution of 3% glutaraldehyde and paraformaldehyde for 2 h. Samples were dehydrated in increasing concentrations of ethanol (30, 50, 70, 80, 90 and 100%), 10 min for each wash. Samples were transferred to hexamethyldisilazane for 1 h and air dried overnight. Samples were sputter coated with 10 nm platinum prior to imaging. SEM imaging was done on the XL30 30 kV Scanning electron microscope.

## RNA isolation and quantitative PCR

For bulk RNA isolation, skin infections were transferred into RNA Tissue Protect buffer, then transferred into Trizol with one sterile stainless steel bead (5 mm) lysed with a Retsch Tissue Lyser for 3 min. RNA was extracted using chloroform and Rneasy mini kit (Qiagen). RNA (0.8 µg) was used for cDNA synthesis with iScript cDNA synthesis kit (Biotech).

For RNA isolation from FACS-sorted monocytes, *Ccr2-creER<sup>T2</sup>; zsGreen<sup>+/-</sup>* mice were treated with 100 mg kg<sup>-1</sup> tamoxifen intraperitoneally for 5 days, with a 2-day washout, then mice were infected with an *S. aureus* bead. At 14 days post-infection, skin infections and spleens were processed into a single-cell suspension and zsGreen<sup>+</sup> monocyte-derived cells were sorted with FACS based on the gating strategy: live CD45<sup>+</sup>CD11b<sup>+</sup>LY6G<sup>-</sup>zsGreen<sup>+</sup>. Samples were sorted directly into Trizol and RNA was isolated as indicated above. RNA input for cDNA synthesis was at max volume due to low RNA concentrations. Monocytes isolated from the spleen served as the internal control for each mouse and RNA expression from skin was normalized to expression from splenic monocytes.

Quantitative PCR was performed using SYBR Green PCR Master Mix (ThermoFisher) on a QuantStudio 6 Real Time PCR System (ThermoFisher). Each sample was run in triplicate and normalized to *Gapdh* and analysed using the delta delta C<sub>t</sub> method. Bulk skin RNA from infections was represented as a fold change over *Ghrl* expression from uninfected skin. FACS-sorted monocyte RNA from skin infections was represented as a fold change over *Ghrl* expression from splenic monocytes of the same animal.

Primers were purchased from Integrated DNA Technologies as Rxn Ready Primer Pools (*Ghrl\_1*: AAGAAGCCACCAGCTAAAC, *Ghrl\_2*: ATCGAAGGGAGCATTGAAC; *GAPDH\_1*: ATCACTGCCACCCAGAAG, *GAPDH\_2*: TCCACGACGGACACATTG). Cycling conditions for quantitative PCR were as follows: (1) hold: 95 °C, 10 min (1×); (2) denature: 95 °C, 15 s and anneal + extend: 55 °C, 1 min (×40); and (3) melt curve, per machine protocol.

## Single-cell RNA-sequencing analysis

The dataset used to probe gene expression of stromal cells in the skin was previously published<sup>18</sup> and is accessible at the Gene Expression Omnibus (GEO) database under accession GSM2910020. To generate this dataset, we used FACS-isolated tdTomato<sup>+</sup> fibroblasts (81%), endothelial cells (13%), pericytes (3%), and other/unknown cells (3%) from *Hic1<sup>CreERT2</sup>; Rosa<sup>tdTomato</sup>* dorsal back skin at P28 (adult second anagen)<sup>18</sup>. For this study, we filtered out other/unknown cells and reclustered all cells that passed Seurat-recommended QC metrics (based on unique molecular identifier counts, gene counts, and percentage of mitochondrial genes). Gene expression was log-normalized and scaled to a factor of 10,000. Each cluster's differentially expressed genes were calculated to manually annotate clusters with their respective identities. Individual genes were queried using Seurat's implementation of *VlnPlot* and *FeaturePlot* functions<sup>35</sup>.

## Study design and statistical analysis

Statistical methods were not used to predetermine sample size. In most experiments, sample size was determined based on previous

studies within the laboratory using these techniques. For intravital microscopy, we were limited by imaging only one mouse at a time, so a minimum of one experimental mouse and one control mouse was imaged per day. Sample size was determined based on prior studies and literature using similar experimental paradigms. In instances where the approach had not previously been used, a minimum of four mice per group was used. All experiments were replicated at least once with similar findings and all replications were successful. For all experiments that required either pharmacological treatment or different infection conditions, mice were randomized. The investigators were not blinded during experiments because treatments and data collection were performed by the same researcher. For image analysis, the images were randomly assigned a key by the researcher and all images were processed using the same workflow, therefore, image analysis was blinded after data collection.

Statistical analyses were performed using Prism 9 (Graphpad Software, v9.1.1). Statistical tests are described for each figure in the figure legend.  $P < 0.05$  was considered statistically significant.

### Reporting summary

Further information on research design is available in the Nature Research Reporting Summary linked to this article.

### Data availability

The single-cell RNA-sequencing dataset analysed in this study is available in the Gene Expression Omnibus under accession code GSM2910020.

27. Dal-Secco, D. et al. A dynamic spectrum of monocytes arising from the in situ reprogramming of CCR2<sup>+</sup> monocytes at a site of sterile injury. *J. Exp. Med.* **212**, 447–456 (2015).
28. Baba, T. et al. Genome and virulence determinants of high virulence community-acquired MRSA. *Lancet* **359**, 1819–1827 (2002).
29. Wang, R. et al. Identification of novel cytolytic peptides as key virulence determinants for community-associated MRSA. *Nat. Med.* **13**, 1510–1514 (2007).
30. Pang, Y. Y. et al. *agr*-Dependent interactions of *Staphylococcus aureus* USA300 with human polymorphonuclear neutrophils. *J. Innate Immun.* **2**, 546–559 (2010).
31. Harding, M. & Kubes, P. Innate immunity in the vasculature: Interactions with pathogenic bacteria. *Curr. Opin. Microbiol.* **15**, 85–91 (2012).
32. McDonald, B. et al. Intravascular danger signals guide neutrophils to sites of sterile inflammation. *Science* **330**, 362–366 (2010).

33. Yipp, B. G. et al. Infection-induced NETosis is a dynamic process involving neutrophil multitasking in vivo. *Nat. Med.* **18**, 1386–1393 (2012).
34. Zwick, R. K. et al. Adipocyte hypertrophy and lipid dynamics underlie mammary gland remodeling after lactation. *Nat. Commun.* **9**, 3592 (2018).
35. Stuart, T. et al. Comprehensive integration of single-cell data. *Cell* **177**, 1888–1902.e1821 (2019).

**Acknowledgements** We thank T. Nussbaumer for mice husbandry and genotyping; R. Gamutin for monitoring infected mice in the University of Calgary biohazard animal facility; P. Colarusso, A. Chojnacki and L. Swift at the University of Calgary Live Cell Imaging Facility for microscope usage and image analysis support; J. Zindel for providing the R scripts for image analysis; W. Y. Lee for microscope assistance and maintenance and assistance with experiments; H. Kuipers for use of the Cytek Aurora, which was funded through the Canadian Foundation for Innovation; P. Mukherjee and the Microscopy and Imaging Facility at the University of Calgary for scanning electron microscopy assistance; Y. Ou and S. Liu and the Alberta Precision Research Laboratories for assistance with histology; B. G. J. Surewaard for providing the *S. aureus* MW2 strain; and T. Kieffer for providing the *Lep<sup>r</sup><sup>fl</sup>* mice. R.M.K. was supported by the Alberta Graduate Excellence Scholarship and the University of Calgary Doctoral Scholarship. H.B.S. and S.S. were supported by CIHR Vanier scholarships. This work was supported by foundation grants from the Canadian Institute of Health Research (FDN148380 to K.A.S. and FDN143248 to P.K.).

**Author contributions** R.M.K., J.F.D. and P.K. designed the experiments. R.M.K., H.B.S., R.S., W.Y.L., E.L., and C.M.K. performed the experiments. Specifically, R.M.K. performed all experiments, with the following exceptions: H.B.S. assisted with operating the confocal microscope (Extended Data Fig. 2i,j) and performed the whole-mount immunofluorescence (Extended Data Fig. 7g), R.S. assisted with mouse treatments and the monocyte sorting for adoptive transfer experiments (Fig. 2l–o), W.Y.L. performed bone marrow transfers (Fig. 4l–p) and assisted with mouse treatments; E.L. performed immunofluorescence and imaging of BODIPY-stained skin sections (Extended Data Fig. 7e) and C.M.K. performed immunofluorescence staining and imaging for Extended Data Fig. 7h. R.M.K. analysed all data except for the scRNA-seq dataset, which was analysed by S.S., J.Y.N. and Y.S. provided ghrelin-deficient bones for bone marrow transfer. B.G.J.S. contributed technical and experimental support for the *S. aureus* infection model and provided critical review of the paper. K.A.S. provided expertise in immunofluorescence staining and critical review of the paper. M.M. provided the MC-21 monocyte-depleting antibody. J.B. supervised the single-cell sequencing analysis. R.M.K., J.F.D. and P.K. wrote the manuscript with input from all co-authors. All authors read and approved the manuscript for submission. J.F.D. and P.K. supervised the study.

**Competing interests** The authors declare no competing interests.

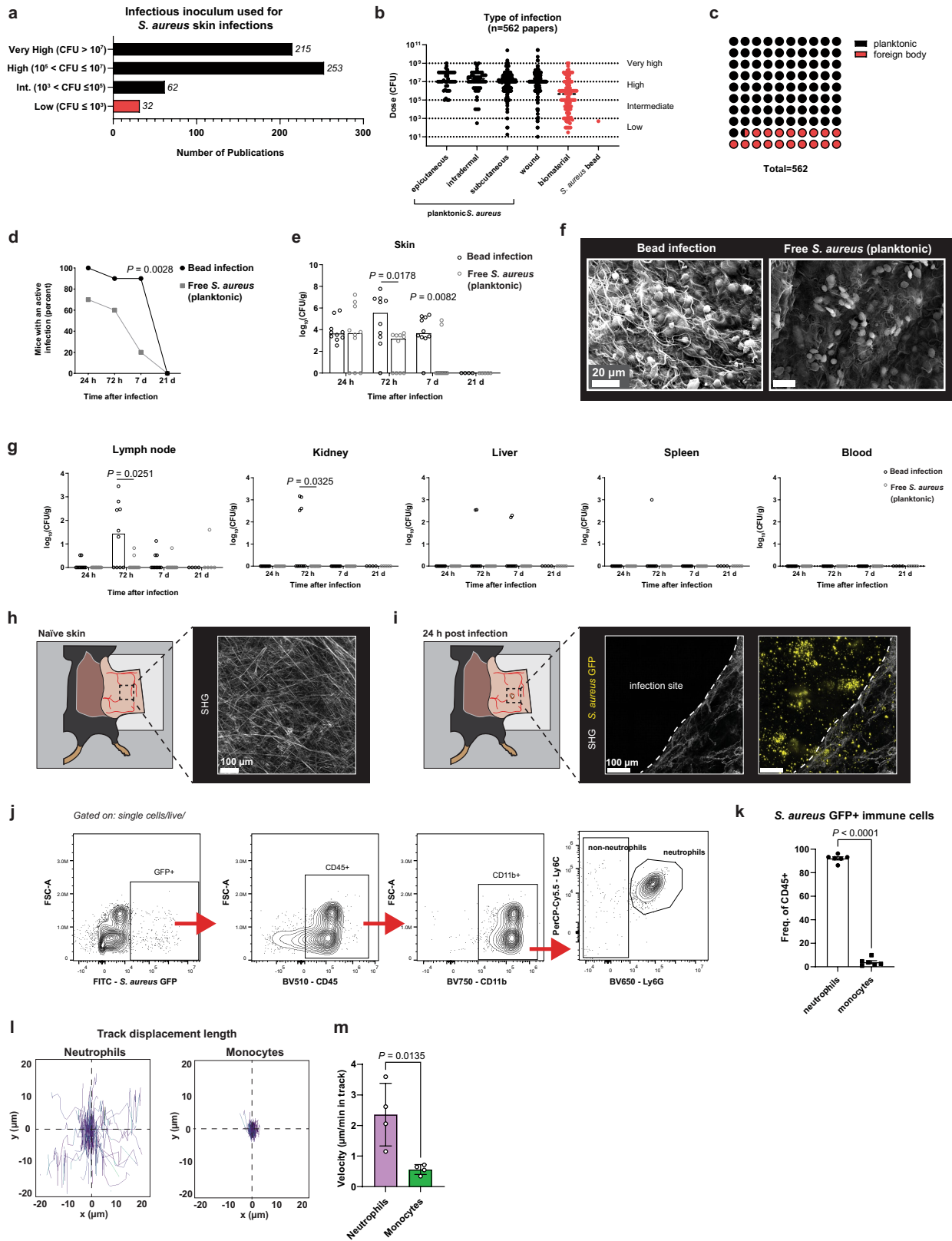
### Additional information

**Supplementary information** The online version contains supplementary material available at <https://doi.org/10.1038/s41586-022-05044-x>.

**Correspondence and requests for materials** should be addressed to Justin F. Deniset or Paul Kubes.

**Peer review information** Nature thanks Vishwa Dixit, Miriam Merad, Victor Torres and the other, anonymous, reviewer for their contribution to the peer review of this work. Peer review reports are available.

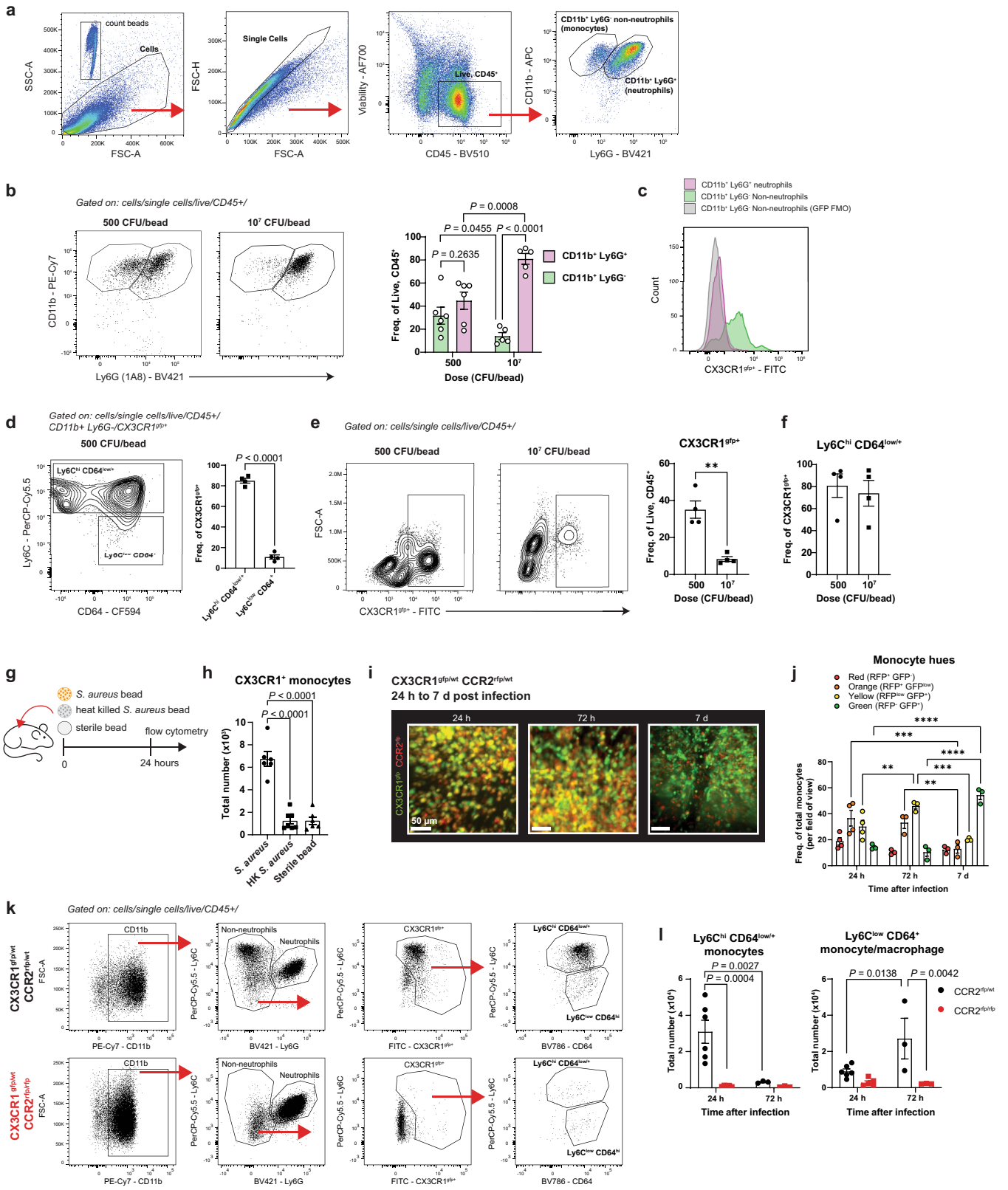
**Reprints and permissions information** is available at <http://www.nature.com/reprints>.



Extended Data Fig. 1 | See next page for caption.

**Extended Data Fig. 1 | Characterization of the *S. aureus* bead infection *in vivo*.** **a–c**, Literature review of infectious dose used to study *S. aureus* skin infections, arranged by low-dose to very high dose (**a**), absolute value for infectious dose for each type of infection (**b**), and proportion of papers that used planktonic vs foreign body-associated *S. aureus* (**c**). **d, e**, C57 mice were infected with low-dose *S. aureus* bead or 500 CFU in 50  $\mu$ L saline (planktonic) and CFUs were measured over time indicated. **d**, Percentage of mice with an active infection with detectable CFUs.  $n = 10$  mice (for 24 h, 72 h, 7 d) and  $n = 5$  (for 21 d) mice per group from 2 independent experiments; two-sided Chi square test at individual time points;  $P = 0.0603$  (24 h),  $P = 0.1213$  (72 h),  $P = 0.0028$  (7 d). **e**, Quantification of skin CFUs post-infection.  $n = 10$  mice (for 24 h, 72 h, 7 d) and  $n = 5$  (for 21 d) mice per group from 2 independent experiments; unpaired two-sided Student *t*-test at individual time points (24 h), unpaired two-sided Mann Whitney U-test between individual time points (72 h, 7 d); data are median;  $P = 0.6470$  (24 h),  $P = 0.0178$  (72 h),  $P = 0.0082$  (7 d). **f**, C57 mice were infected with low-dose *S. aureus* bead or 500 CFU in 50  $\mu$ L saline (planktonic) and skin infections were processed for scanning electron microscopy at 24 h. Representative image of bead and planktonic infection. Image representative from  $n = 3$  mice per group from 2 independent experiments. **g**, C57 mice were infected with low-dose *S. aureus* bead or 500 CFU in 50  $\mu$ L saline (planktonic) and CFUs were measured over time indicated. Quantification of CFUs in skin-draining lymph node, kidney, liver, spleen, and

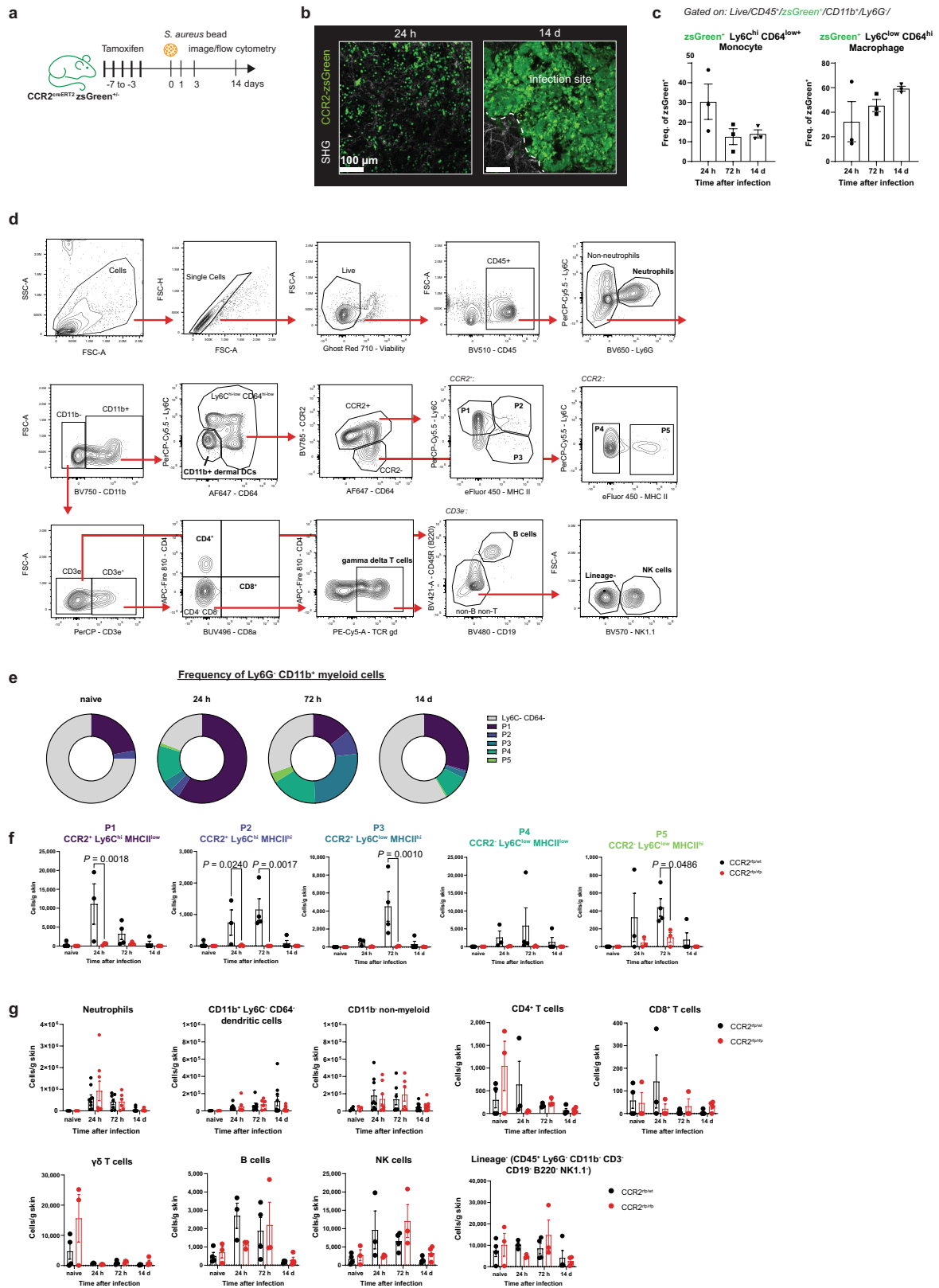
blood.  $n = 10$  mice (for 24 h, 72 h, 7 d) and  $n = 5$  (for 21 d) mice per group from 2 independent experiments; unpaired two-sided Mann Whitney U-test between individual time points; data are median; LN 72h:  $P = 0.0251$ , Kidney 72 h:  $P = 0.0325$ , all other groups  $P > 0.05$ . **h**, Representative image of naïve skin in wildtype mice, representative of  $n = 3$  mice from 2 independent experiments. Scale bar, 100  $\mu$ m. **i**, Representative image of a 24 h infection in wildtype mice infected with GFP-expressing MW2 *S. aureus* bead, representative of  $n = 3$  mice from 2 independent experiments. Infection site is highlighted with a dashed line. Scale bar, 100  $\mu$ m. **j, k**, C57 mice were infected with GFP-expressing *S. aureus* bead and flow cytometry was performed at 24 h. **j**, Gating strategy to identify immune cells positive for GFP<sup>+</sup> *S. aureus*. **k**, Quantification of *S. aureus* GFP<sup>+</sup> immune cells shown as frequency of CD45<sup>+</sup> cells.  $n = 6$  mice per group from 2 independent experiments; unpaired two-sided Student *t*-test; data are mean  $\pm$  s.e.m.;  $P < 0.0001$ . **l, m**, *Cx3cr1*<sup>GFP/+</sup> Catchup<sup>ivm-red</sup> mice were infected with low-dose *S. aureus* bead and monocyte and neutrophil behaviour was imaged *in vivo* at 24 h post-infection. **l**, Representative spider plot showing track displacement length of CX3CR1<sup>8fp+</sup> monocytes and tdTomato<sup>+</sup> neutrophils at the site of infection over a 20-minute time-lapse video. Plots are representative of  $n = 4$  mice per group from 2 independent experiments. **m**, Quantification of the average velocity of neutrophils and CX3CR1<sup>8fp+</sup> cells.  $n = 4$  mice per group from 2 independent experiments; unpaired two-sided Student *t*-test; data are mean  $\pm$  s.e.m.;  $P = 0.0135$ .



Extended Data Fig. 2 | See next page for caption.

**Extended Data Fig. 2 | Assessment of immune cell recruitment to *S. aureus* skin infection at 24 h post-infection.** **a-f**, *Cx3cr1<sup>GFP/+</sup> Ccr2<sup>RFP/+</sup>* mice were infected with low (500 CFU/bead) or high (10<sup>7</sup> CFU/bead) dose *S. aureus* bead and flow cytometry was performed at 24 h. **a**, Gating strategy to identify immune cell populations. **b**, Representative flow cytometry plots and quantification of CD11b<sup>+</sup> Ly6G<sup>+</sup> neutrophils and CD11b<sup>+</sup> Ly6G<sup>-</sup> non-neutrophils at low and high dose bead. Quantification shown as frequency of Live, CD45<sup>+</sup> cells. *n* = 5 mice (high dose) and *n* = 6 mice (low-dose) from 2 independent experiments; mixed-effects analysis with Šidák's multiple comparisons test; data are mean ± s.e.m.; *P* = 0.2635 (low-dose CD11b<sup>+</sup> Ly6G<sup>+</sup> vs low-dose CD11b<sup>+</sup> Ly6G<sup>-</sup>), *P* < 0.0001 (high dose CD11b<sup>+</sup> Ly6G<sup>+</sup> vs high dose CD11b<sup>+</sup> Ly6G<sup>-</sup>), *P* = 0.0008 (CD11b<sup>+</sup> Ly6G<sup>+</sup> low-dose vs CD11b<sup>+</sup> Ly6G<sup>+</sup> high dose), *P* = 0.0455 (CD11b<sup>+</sup> Ly6G<sup>-</sup> low-dose vs CD11b<sup>+</sup> Ly6G<sup>-</sup> high dose). **c**, Representative histogram of CX3CR1<sup>gfp</sup> expression in CD11b<sup>+</sup> Ly6G<sup>+</sup> neutrophils, CD11b<sup>+</sup> Ly6G<sup>-</sup> non-neutrophils, and non-neutrophils from GFP FMO control. **d**, Representative flow cytometry plot showing expression of LY6C and CD64 gated on single cells/live/CD45<sup>+</sup>/CD11b<sup>+</sup> Ly6G<sup>-</sup>/CX3CR1<sup>gfp</sup> cells, showing populations of GFP<sup>+</sup> LY6C<sup>hi</sup> CD64<sup>low/+</sup> monocytes and GFP<sup>+</sup> LY6C<sup>low</sup> CD64<sup>+</sup> macrophages recruited to low-dose *S. aureus* bead. Quantification shown as frequency of CX3CR1<sup>gfp</sup> cells. *n* = 4 mice per group, data representative from 2 independent experiments; unpaired two-sided Student *t*-test; data are mean ± s.e.m.; *P* < 0.0001. **e**, Representative flow cytometry plots showing expression of CX3CR1<sup>gfp</sup> cells gated on single cells/live/CD45<sup>+</sup> cells. Quantification of total CX3CR1<sup>gfp</sup> cells shown as frequency of live, CD45<sup>+</sup> cells. *n* = 4 mice per group, data representative from 2 independent experiments; unpaired two-sided Student *t*-test; data are mean ± s.e.m.; *P* = 0.0015. **f**, Quantification of GFP<sup>+</sup> LY6C<sup>hi</sup> CD64<sup>low/+</sup> monocytes shown as frequency of live/CD45<sup>+</sup>/CX3CR1<sup>gfp</sup> cells in high and low-dose *S. aureus* bead. unpaired two-sided Student *t*-test; data are mean ± s.e.m.; *P* = 0.6772. **g, h**, C57 mice were infected with *S. aureus* bead, heat-

killed *S. aureus* bead or sterile bead and flow cytometry was performed at 24 h. **g**, Experiment timeline. **h**, Quantification of total numbers of CX3CR1<sup>+</sup> myeloid cells gated from single cells/live/CD45<sup>+</sup>/CD11b<sup>+</sup>/LY6G<sup>-</sup>. *n* = 6 mice (*S. aureus*, sterile bead) and *n* = 7 mice (heat-killed *S. aureus*) from 2 independent experiments; one-way ANOVA with Tukey's multiple comparisons test; data are mean ± s.e.m.; *P* < 0.0001. **i, j**, *Cx3cr1<sup>GFP/+</sup> Ccr2<sup>RFP/+</sup>* mice were infected with *S. aureus* bead and imaged with spinning disk confocal intravital microscopy at 24 h, 72 h, and 7 d post-infection. **i**, Representative images showing monocyte heterogeneity during infection, representative of *n* = 4 mice (24 h) and 3 mice (72 h, 7 d) per group from 4 independent experiments. **j**, Quantification of the average intensity of GFP and RFP expression in monocytes. Each dot represents the average of 3 FOV from one mouse. *n* = 4 mice (24 h) and 3 mice (72 h, 7 d) per group from 4 independent experiments; mixed effects analysis with Šidák's multiple comparisons test; data are mean ± s.e.m.; \*\**P* < 0.01, \*\*\**P* < 0.001, \*\*\*\**P* < 0.0001. **k, l**, *Cx3cr1<sup>GFP/+</sup> Ccr2<sup>RFP/+</sup>* and *Cx3cr1<sup>GFP/+</sup> Ccr2<sup>RFP/RFP</sup>* mice were infected with *S. aureus* bead and flow cytometry was run at 24 h and 72 h. **k**, Gating strategy used to identify CX3CR1<sup>gfp</sup> monocyte populations. **l**, Quantification of total numbers of CX3CR1<sup>gfp</sup> LY6C<sup>hi</sup> CD64<sup>low/+</sup> and CX3CR1<sup>gfp</sup> LY6C<sup>low</sup> CD64<sup>hi</sup> monocytes/macrophages. *n* = 6 mice (24 h) and 3 mice (72 h) per group from 2 independent experiments; two-way ANOVA with Šidák's multiple comparison; data are mean ± s.e.m.; For CX3CR1<sup>gfp</sup> LY6C<sup>hi</sup> CD64<sup>low/+</sup>: *P* = 0.0027 (*Cx3cr1<sup>GFP/+</sup> Ccr2<sup>RFP/+</sup>* 24h vs *Cx3cr1<sup>GFP/+</sup> Ccr2<sup>RFP/+</sup>* 72h), *P* = 0.9980 (*Cx3cr1<sup>GFP/+</sup> Ccr2<sup>RFP/RFP</sup>* 24 h vs *Cx3cr1<sup>GFP/+</sup> Ccr2<sup>RFP/RFP</sup>* 72h), *P* = 0.0004 (*Cx3cr1<sup>GFP/+</sup> Ccr2<sup>RFP/+</sup>* 24 h vs *Cx3cr1<sup>GFP/+</sup> Ccr2<sup>RFP/RFP</sup>* 24 h), *P* = 0.9390 (*Cx3cr1<sup>GFP/+</sup> Ccr2<sup>RFP/+</sup>* 72 h vs *Cx3cr1<sup>GFP/+</sup> Ccr2<sup>RFP/RFP</sup>* 72 h); For CX3CR1<sup>gfp</sup> LY6C<sup>low</sup> CD64<sup>hi</sup>: *P* = 0.0138 (*Cx3cr1<sup>GFP/+</sup> Ccr2<sup>RFP/+</sup>* 24 h vs *Cx3cr1<sup>GFP/+</sup> Ccr2<sup>RFP/+</sup>* 72 h), *P* = 0.9923 (*Cx3cr1<sup>GFP/+</sup> Ccr2<sup>RFP/RFP</sup>* 24 h vs *Cx3cr1<sup>GFP/+</sup> Ccr2<sup>RFP/RFP</sup>* 72 h), *P* = 0.3943 (*Cx3cr1<sup>GFP/+</sup> Ccr2<sup>RFP/+</sup>* 24 h vs *Cx3cr1<sup>GFP/+</sup> Ccr2<sup>RFP/RFP</sup>* 24 h), *P* = 0.0042 (*Cx3cr1<sup>GFP/+</sup> Ccr2<sup>RFP/RFP</sup>* 72 h vs *Cx3cr1<sup>GFP/+</sup> Ccr2<sup>RFP/RFP</sup>* 72 h).



Extended Data Fig. 3 | See next page for caption.

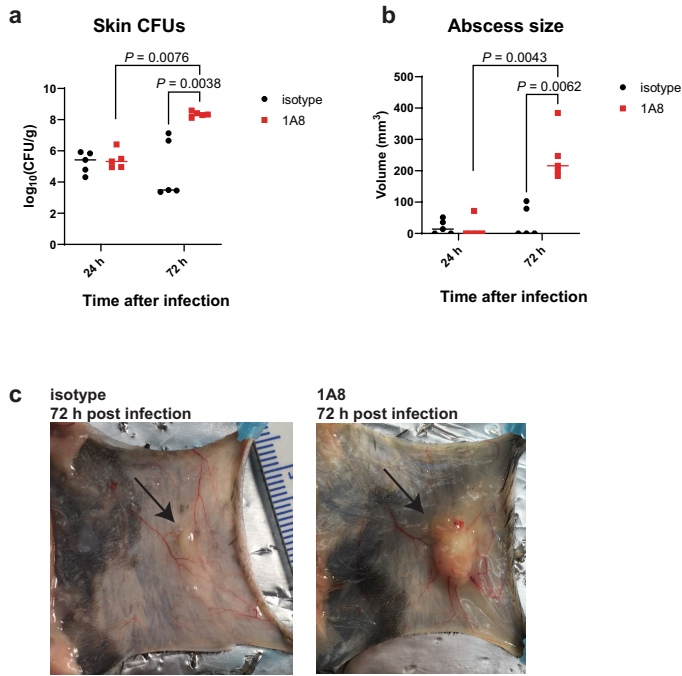
**Extended Data Fig. 3 | Characterization of monocyte/macrophage**

**populations at the *S. aureus* skin infection. a-c, *CCR2-creER<sup>T2</sup>;zsGreen<sup>+/-</sup>* mice were treated with tamoxifen, infected with low-dose *S. aureus* bead, and imaged or processed for flow cytometry analysis at indicated time points.**

**a, Experiment timeline for fate mapping with *CCR2-creER<sup>T2</sup>;zsGreen<sup>+/-</sup>* mice.**

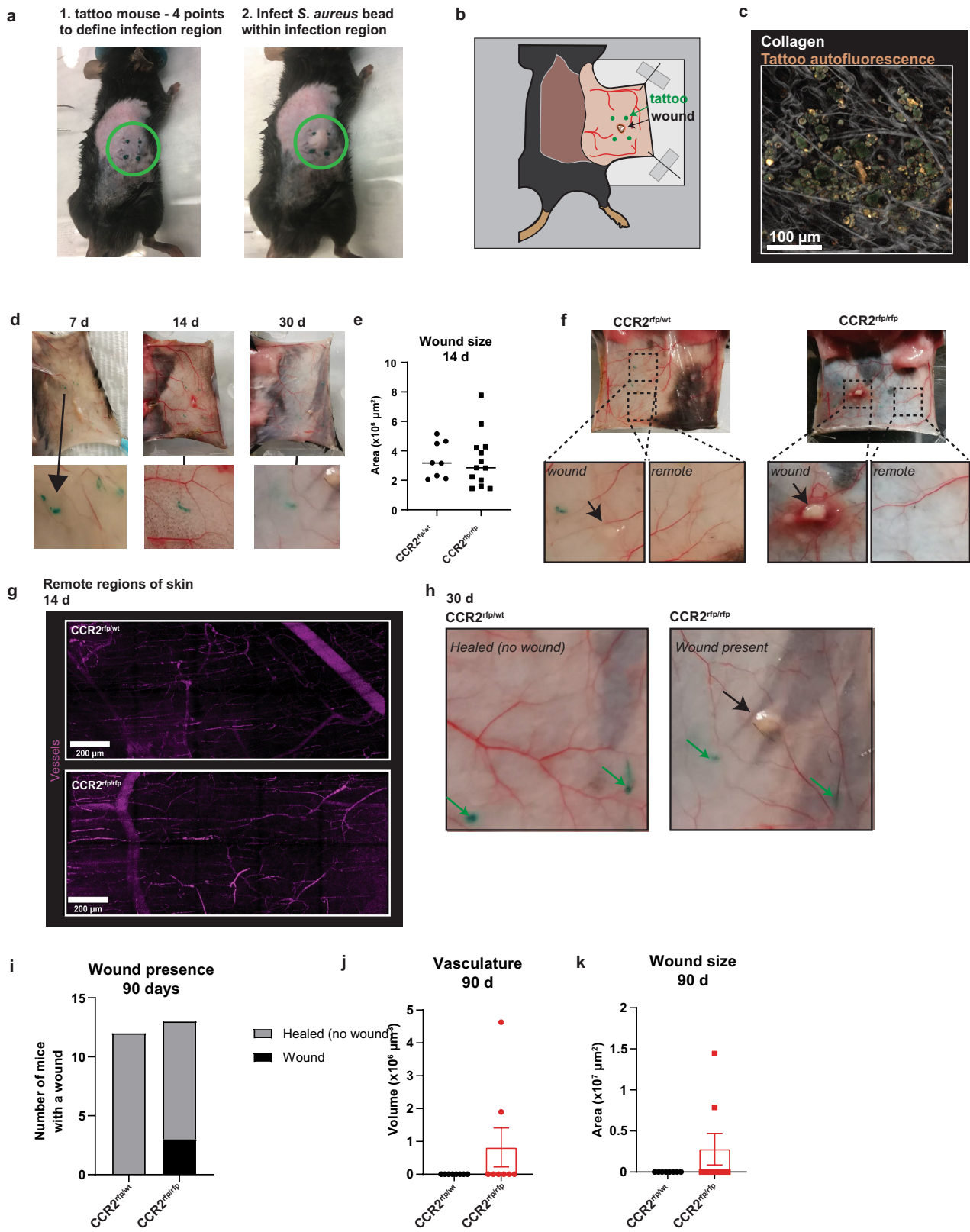
**b, Representative image of zsGreen<sup>+</sup> cells recruited to the *S. aureus* skin infection at 24 h and 14 d post-infection. Infection site is highlighted with a dashed line. Image representative of  $n = 3$  mice per group from 2 independent experiments. Scale bar, 100  $\mu\text{m}$ . **c, Quantification of zsGreen<sup>+</sup> LY6C<sup>hi</sup> CD64<sup>low/+</sup> monocytes and zsGreen<sup>+</sup> LY6C<sup>low</sup> CD64<sup>+</sup> macrophages shown as frequency of zsGreen<sup>+</sup> cells.  $n = 3$  mice per group from 2 independent experiments, one-way ANOVA with Tukey's multiple comparison test; data are mean  $\pm$  s.e.m.; For zsGreen<sup>+</sup> LY6C<sup>hi</sup> CD64<sup>low/+</sup>,  $P = 0.1570$  (24 h vs 72 h),  $P = 0.1965$  (24 h vs 14 d),  $P = 0.9829$  (72 h vs 14 d); For zsGreen<sup>+</sup> LY6C<sup>low</sup> CD64<sup>+</sup>:  $P = 0.6387$  (24 h vs 72 h),  $P = 0.2125$  (24 h vs 14 d),  $P = 0.6115$  (72 h vs 14 d). **d-g, *Ccr2<sup>RFP/+</sup>* and *Ccr2<sup>RFP/RFP</sup>* mice were infected with *S. aureus* bead and skin infections were processed for spectral flow cytometry analysis of monocyte/macrophage populations at indicated time points. **d, Gating strategy used to identify immune cell populations isolated from skin infections. **e, Pie chart representing the proportion of monocyte subsets in *Ccr2<sup>RFP/+</sup>* mice shown as frequency of LY6G<sup>-</sup>**********

CD11b<sup>+</sup> myeloid cells. **f, Quantification of total numbers of P1-P5 monocyte/macrophage subsets in *Ccr2<sup>RFP/+</sup>* and *Ccr2<sup>RFP/RFP</sup>* mice.  $n = 4$  mice (*Ccr2<sup>RFP/+</sup>*: naïve, 72 h, 14 d; *Ccr2<sup>RFP/RFP</sup>*: 14 d) and 3 mice (*Ccr2<sup>RFP/+</sup>*: 24 h; *Ccr2<sup>RFP/RFP</sup>*: naïve, 24 h, 72 h) per group from 3 independent experiments; mixed effects analysis with Šidák's multiple comparisons test; data are mean  $\pm$  s.e.m.; For P1:  $P = 0.0018$  (*Ccr2<sup>RFP/+</sup>* 24 h vs *Ccr2<sup>RFP/RFP</sup>* 24 h); For P2:  $P = 0.0240$  (*Ccr2<sup>RFP/+</sup>* 24 h vs *Ccr2<sup>RFP/RFP</sup>* 24 h);  $P = 0.0017$  (*Ccr2<sup>RFP/+</sup>* 72 h vs *Ccr2<sup>RFP/RFP</sup>* 72 h); For P3:  $P = 0.0010$  (*Ccr2<sup>RFP/+</sup>* 72 h vs *Ccr2<sup>RFP/RFP</sup>* 72 h); For P5:  $P = 0.0486$  (*Ccr2<sup>RFP/+</sup>* 72 h vs *Ccr2<sup>RFP/RFP</sup>* 72 h); All other groups  $P > 0.05$ . **g, Quantification of total numbers immune cell populations in *Ccr2<sup>RFP/+</sup>* and *Ccr2<sup>RFP/RFP</sup>* mice. For quantification of neutrophils, CD11b<sup>+</sup> dendritic cells, CD11b non-myeloid cells:  $n = 4$  mice (*Ccr2<sup>RFP/+</sup>*: naïve), 3 mice (*Ccr2<sup>RFP/RFP</sup>*: naïve), 9 mice (*Ccr2<sup>RFP/+</sup>*: 24 h), 8 mice (*Ccr2<sup>RFP/RFP</sup>*: 24 h), 7 mice (*Ccr2<sup>RFP/+</sup>*: 72 h), 6 mice (*Ccr2<sup>RFP/RFP</sup>*: 72 h), 9 mice (*Ccr2<sup>RFP/+</sup>*: 14 d) and 11 mice (*Ccr2<sup>RFP/RFP</sup>*: 14 d) per group from 5 independent experiments. For quantification of CD4<sup>+</sup> T cells, CD8<sup>+</sup> T cells,  $\lambda\delta$  T cells, B cells, NK cells and Lin<sup>-</sup> cells:  $n = 4$  mice (*Ccr2<sup>RFP/+</sup>*: naïve, 72 h, 14 d; *Ccr2<sup>RFP/RFP</sup>*: 14 d) and 3 mice (*Ccr2<sup>RFP/+</sup>*: 24 h; *Ccr2<sup>RFP/RFP</sup>*: naïve, 24 h, 72 h) per group from 3 independent experiments. mixed effects analysis with Šidák's multiple comparisons test; data are mean  $\pm$  s.e.m.;  $P > 0.05$  (for all groups at all time points for *Ccr2<sup>RFP/+</sup>* vs *Ccr2<sup>RFP/RFP</sup>*).****



**Extended Data Fig. 4 | Neutrophil depletion results in significant CFU**

**burden in skin at 72 h post-infection.** **a-c**, C57/BL6 mice were treated with neutrophil depleting antibody (LY6G 1A8) or isotype control antibody (2A3) and infected with low-dose *S. aureus* bead. **a**, Quantification of bacterial CFUs from skin at 24 and 72 h.  $n = 5$  mice per time point from 2 independent experiments; two-way ANOVA with Šidák's multiple comparisons test; data are mean  $\pm$  s.e.m.;  $P = 0.9335$  (24 h 2A3 vs 24 h 1A8),  $P = 0.0038$  (72 h 2A3 vs 72 h 1A8),  $P = 0.6611$  (24 h 2A3 vs 72 h 2A3),  $P = 0.0076$  (24 h 1A8 vs 72 h 1A8). **b**, Quantification of abscess size at 24 and 72 h.  $n = 5$  mice per time point from 2 independent experiments; two-way ANOVA with Šidák's multiple comparisons test; data are mean  $\pm$  s.e.m.;  $P = 0.9831$  (24 h 2A3 vs 24 h 1A8),  $P = 0.0062$  (72 h 2A3 vs 72 h 1A8),  $P = 0.8751$  (24 h 2A3 vs 72 h 2A3),  $P = 0.0043$  (24 h 1A8 vs 72 h 1A8). **c**, Representative image of a 72 h infection in isotype or 1A8-treated mouse.

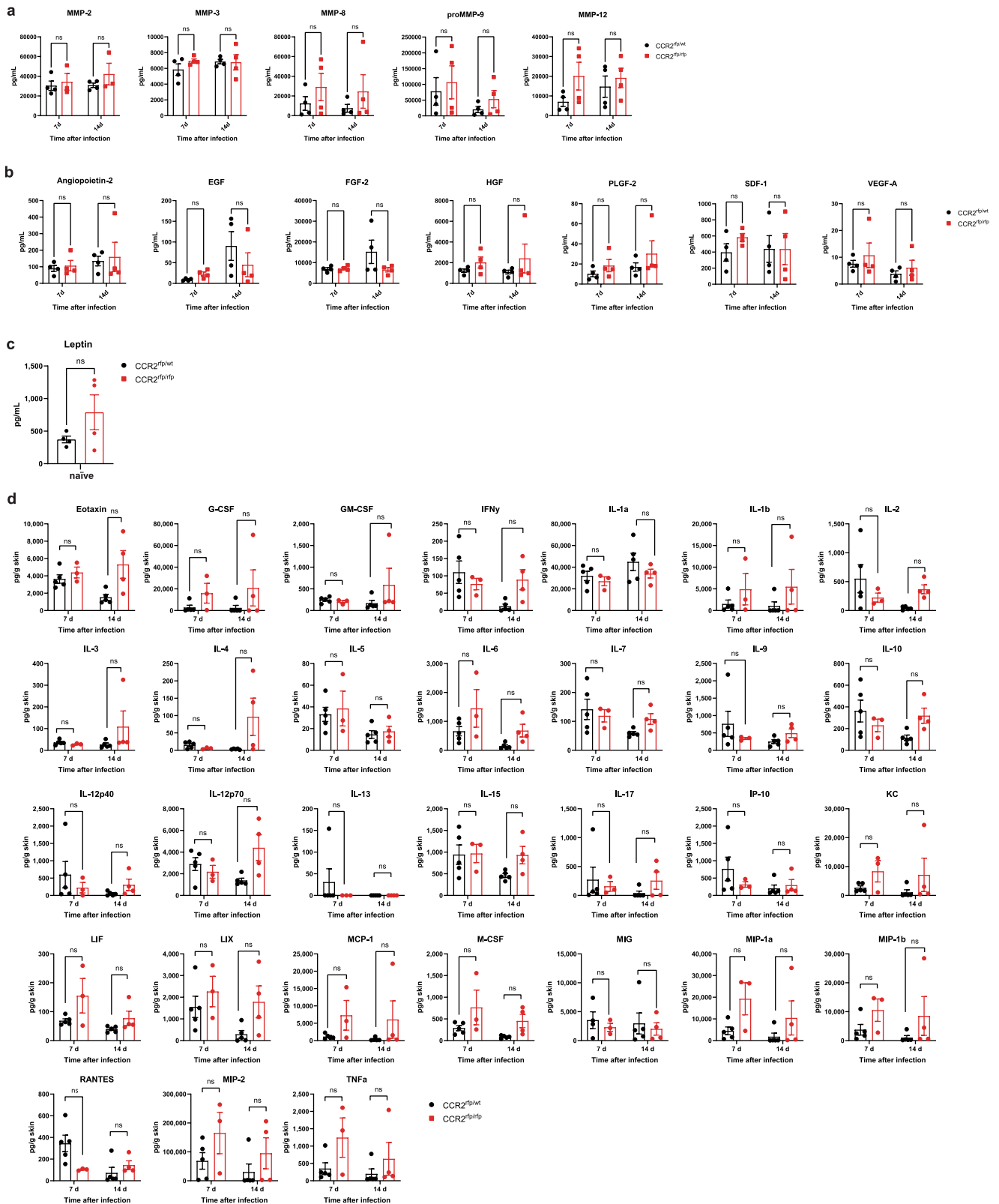


Extended Data Fig. 5 | See next page for caption.

# Article

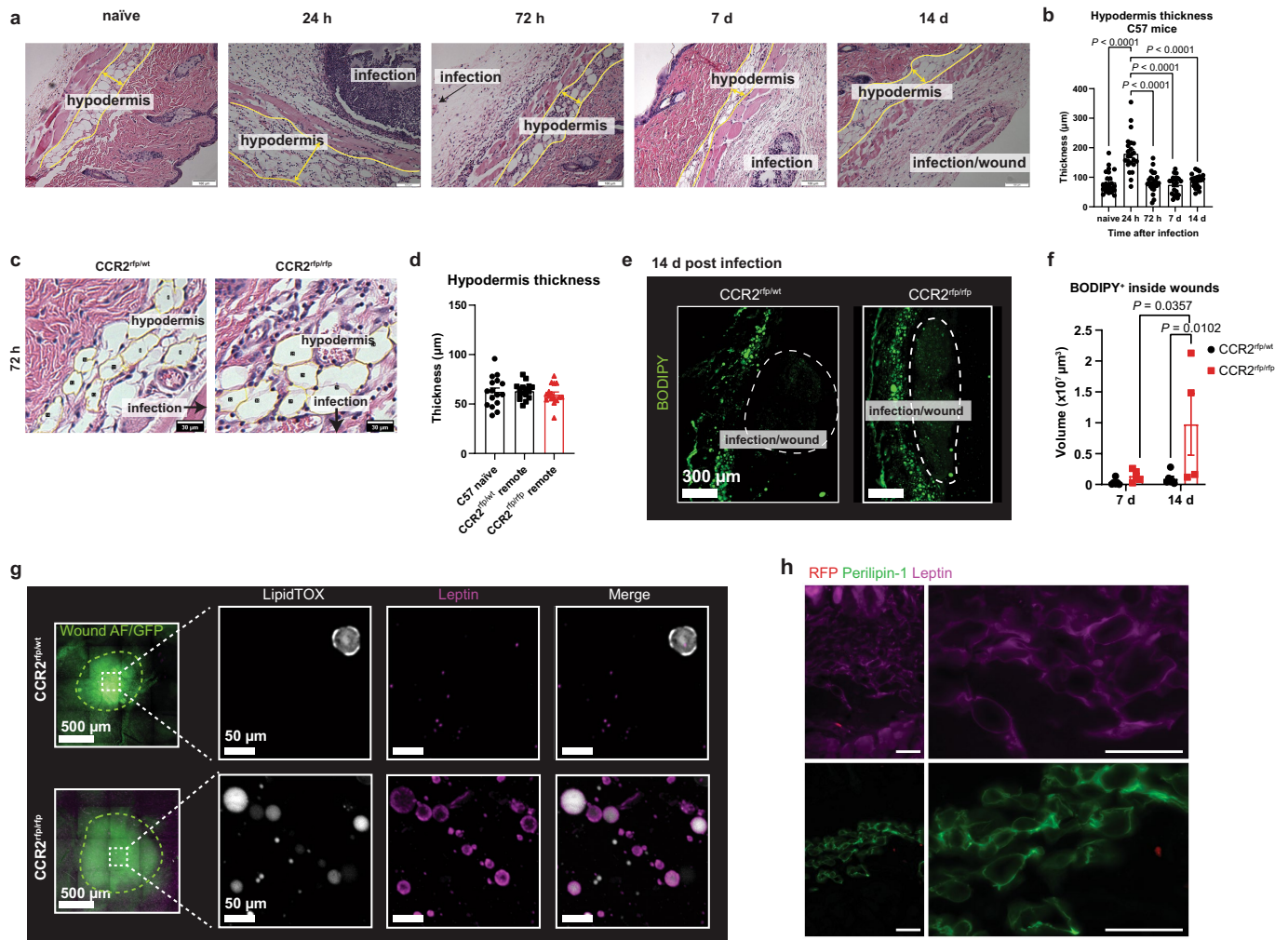
**Extended Data Fig. 5 | A tattoo identifies the infection region over 30 days.**  
**a–d**, Mice were tattooed with green tattoo ink prior to infection with low-dose *S. aureus* bead. **a**, Representative photo of a mouse with tattoo prior to infection with *S. aureus* bead (left) and immediately after injection of the *S. aureus* bead (right). **b**, Diagram showing placement of tattoo around *S. aureus* infection/wound. **c**, Representative intravital image of autofluorescent tattoo ink in skin. Scale bar, 100  $\mu\text{m}$ . **d**, Representative photos of the tattoo points visible in mouse skin at 7 d, 14 d and 30 d post-infection. **e–g**,  $Ccr2^{RFP/+}$  and  $Ccr2^{RFP/RFP}$  mice were infected with low-dose *S. aureus* bead and imaged at 14 days post-infection. **e**, Quantification of wound size.  $n = 8$  for  $Ccr2^{RFP/+}$  and  $n = 13$  for  $Ccr2^{RFP/RFP}$  mice from 6 independent experiments. **f**, Representative photos of a wound from  $Ccr2^{RFP/+}$  and  $Ccr2^{RFP/RFP}$  mice at 14 days post-infection. Black

arrow points to wound. **g**, Representative intravital images showing 3D projection of vasculature in remote regions of skin at 14 days post-infection in  $Ccr2^{RFP/+}$  (top) and  $Ccr2^{RFP/RFP}$  (bottom) mice. Scale bar, 200  $\mu\text{m}$ . Images representative of  $n = 7$  for  $Ccr2^{RFP/+}$  and  $n = 12$  for  $Ccr2^{RFP/RFP}$  mice from 6 independent experiments. **h**, Representative photos of a healed infection from a  $Ccr2^{RFP/+}$  mouse and a wound present from a  $Ccr2^{RFP/RFP}$  mouse at 30 days post-infection. Green arrows point to tattoo markings in skin. **i–k**,  $Ccr2^{RFP/+}$  and  $Ccr2^{RFP/RFP}$  mice were infected with low-dose *S. aureus* bead and imaged at 90 days post-infection. Quantification of wound presence (**i**), vasculature (**j**), and wound size (**k**) at 90 days post-infection in  $Ccr2^{RFP/+}$  and  $Ccr2^{RFP/RFP}$  mice. For **j–k**,  $n = 12$  mice ( $Ccr2^{RFP/+}$ ) and  $n = 13$  mice ( $Ccr2^{RFP/RFP}$ ) from 2 independent experiments; data are mean  $\pm$  s.e.m.



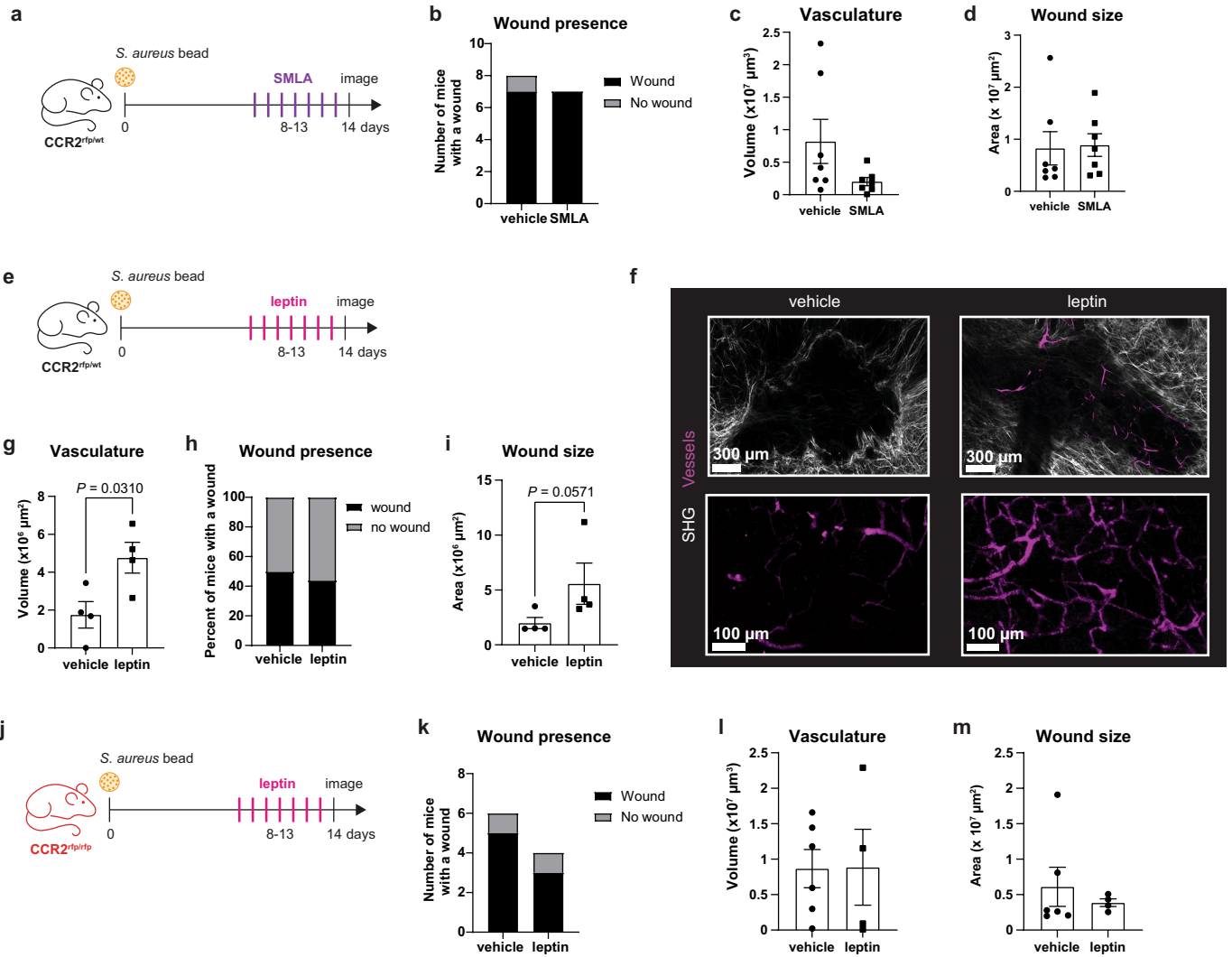
**Extended Data Fig. 6 | Measurement of cytokines by ELISA. a-e**, *Ccr2*<sup>RFP/wt</sup> and *Ccr2*<sup>RFP/RFP</sup> mice were infected with *S. aureus* bead and skin homogenates were analyzed for multiplex ELISA at indicated time points. **a, b**, Multiplex ELISA of matrix metalloproteinases MMP-2, MMP-3, MMP8, proMMP-9 and MMP-12 (**a**), growth factors and repair mediators Angiopoietin-2, EGF, FGF-2, HGF, PLGF-2, SDF-1 and VEGF-A (**b**) from skin homogenates of *Ccr2*<sup>RFP/wt</sup> and *Ccr2*<sup>RFP/RFP</sup> mice at 7- and 14-days post-infection. For **a-b**,  $n = 4$  mice per group from 2 independent experiments; data are mean  $\pm$  s.e.m.; two-way ANOVA with Šidák's multiple comparisons test;  $P > 0.05$  (*Ccr2*<sup>RFP/wt</sup> vs *Ccr2*<sup>RFP/RFP</sup> at all time points for all

mediators). **c**, Measurement of Leptin from naive skin of *Ccr2*<sup>RFP/wt</sup> and *Ccr2*<sup>RFP/RFP</sup> mice.  $n = 4$  per group from 2 independent experiments; unpaired two-sided Student *t*-test; data are mean  $\pm$  s.e.m.;  $P = 0.1769$ . **d**, Measurement of pro- and anti-inflammatory cytokines from skin homogenates of *Ccr2*<sup>RFP/wt</sup> and *Ccr2*<sup>RFP/RFP</sup> mice at 7- and 14-days post-infection.  $n = 6$  mice (*Ccr2*<sup>RFP/wt</sup>, 7 d and 14 d),  $n = 3$  mice (*Ccr2*<sup>RFP/RFP</sup> 7 d), and  $n = 5$  mice (*Ccr2*<sup>RFP/RFP</sup> 14 d) from 2 independent experiments; Mixed effects model with Šidák's multiple comparisons test; data are mean  $\pm$  s.e.m.;  $P > 0.05$  (*Ccr2*<sup>RFP/wt</sup> vs *Ccr2*<sup>RFP/RFP</sup> at all time points for all mediators).



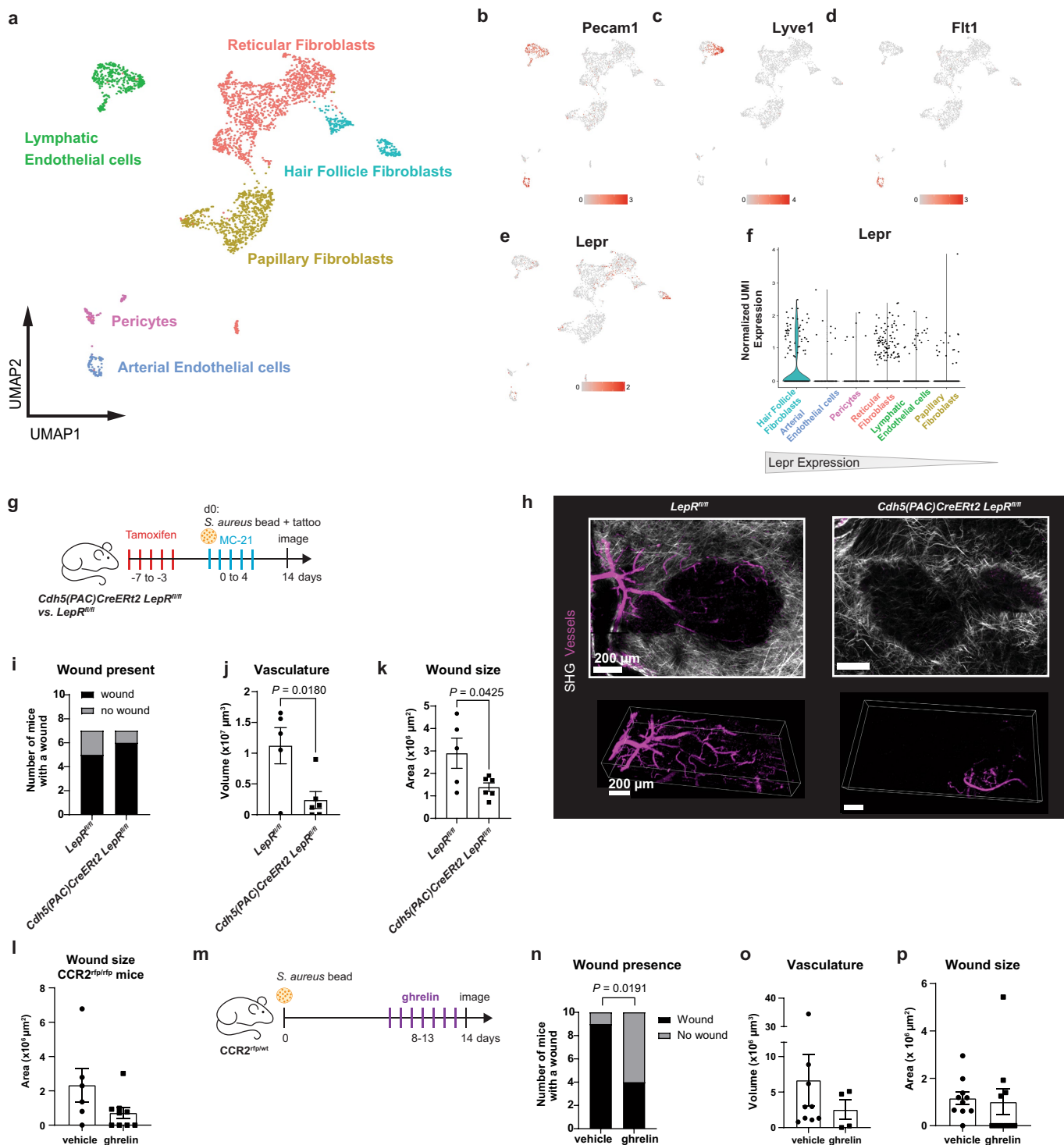
**Extended Data Fig. 7 | Dynamic hypodermal expansion and resolution during *S. aureus* skin infection in wildtype mice.** **a**, C57 mice were infected with low-dose *S. aureus* bead and skin infections were processed for H&E staining at indicated time points. **a**, Representative H&E staining in skin infections. Infection and hypodermis are identified with a label. Scale bar, 100  $\mu\text{m}$ . **b**, Quantification of hypodermis thickness in C57 mice after infection with *S. aureus* bead.  $n = 7$ -8 measurements for each mouse, 3 mice per group, 2 independent experiments; one-way ANOVA with Tukey's multiple comparisons test; data are mean  $\pm$  s.e.m.;  $P < 0.0001$  (for 24 h vs. naive, 24 h vs 72 h, 24 h vs 7 d, 24 h vs 14 d);  $P > 0.05$  (all other groups). **c**, **d**, *Ccr2*<sup>RFP/+</sup> and *Ccr2*<sup>RFP/RFP</sup> mice were infected with low-dose *S. aureus* bead and skin infections were processed for H&E staining at indicated time points. **c**, Representative H&E images of hypodermal adipocyte size in *Ccr2*<sup>RFP/+</sup> and *Ccr2*<sup>RFP/RFP</sup> mice at 72 h post-infection. Scale bar, 30  $\mu\text{m}$ . **d**, Quantification of hypodermis thickness in naive C57 mice versus remote regions of the skin of *Ccr2*<sup>RFP/+</sup> and *Ccr2*<sup>RFP/RFP</sup> mice at 24 h post-infection.  $n = 16$  measurements from 4 mice per group from 2 independent experiments; one-way ANOVA with Tukey's multiple comparisons test; data are mean  $\pm$  s.e.m.;  $P > 0.05$  (all groups). **e**, **f**, *Ccr2*<sup>RFP/+</sup> and *Ccr2*<sup>RFP/RFP</sup>

mice were infected with low-dose *S. aureus* bead and skin infections were processed for BODIPY staining by immunofluorescence. **e**, Representative confocal immunofluorescence of skin sections showing BODIPY<sup>+</sup> adipocytes and lipid droplets in *Ccr2*<sup>RFP/+</sup> and *Ccr2*<sup>RFP/RFP</sup> mice at 14 days post-infection with *S. aureus* bead. Scale bar, 300  $\mu\text{m}$ . **f**, Quantification of total BODIPY<sup>+</sup> signal in the wounds of *Ccr2*<sup>RFP/+</sup> and *Ccr2*<sup>RFP/RFP</sup> mice at 14 days post-infection.  $n = 6$  mice (*Ccr2*<sup>RFP/+</sup>: 7 d, 14 d), 5 mice (*Ccr2*<sup>RFP/RFP</sup>: 7 d) and 4 mice (*Ccr2*<sup>RFP/RFP</sup>: 14 d) per group from 2 independent experiments; data are mean  $\pm$  s.e.m.;  $P = 0.9688$  (*Ccr2*<sup>RFP/+</sup> 7 d vs *Ccr2*<sup>RFP/+</sup> 14 d),  $P = 0.90357$  (*Ccr2*<sup>RFP/RFP</sup> 7 d vs *Ccr2*<sup>RFP/RFP</sup> 14 d),  $P = 0.9097$  (*Ccr2*<sup>RFP/+</sup> 7 d vs *Ccr2*<sup>RFP/RFP</sup> 7 d),  $P = 0.0102$  (*Ccr2*<sup>RFP/+</sup> 14 d vs *Ccr2*<sup>RFP/RFP</sup> 14 d). **g**, *Ccr2*<sup>RFP/+</sup> and *Ccr2*<sup>RFP/RFP</sup> mice were infected with low-dose *S. aureus* bead and skin infections were processed at 14 d for whole mount immunofluorescent staining for leptin and LipidTOX. Representative whole mount images of 14-day wounds from *Ccr2*<sup>RFP/+</sup> and *Ccr2*<sup>RFP/RFP</sup> mice. Scale bars, 500  $\mu\text{m}$  (left) and 50  $\mu\text{m}$  (inset). Image representative of  $n = 3$  mice per group from 2 independent experiments. **h**, Representative immunofluorescence staining for perilipin-1 and leptin in *Ccr2*<sup>RFP/RFP</sup> skin at 14 days post-infection. Scale bars, 50  $\mu\text{m}$ . Image representative of  $n = 3$  mice per group from 2 independent experiments.



**Extended Data Fig. 8 | Leptin stimulates angiogenesis following *S. aureus* skin infection.** **a-d**, *Ccr2*<sup>RFP/wt</sup> mice were infected with low-dose *S. aureus* bead, treated with vehicle or SMLA, and imaged at 14 days post-infection. **a**, Experiment timeline showing SMLA treatment to *Ccr2*<sup>RFP/wt</sup> mice. **b**, Quantification of wound presence. **c**, Quantification of vasculature volume. **d**, Quantification of wound size at 14 d. For (b-d),  $n = 8$  (vehicle) and  $n = 7$  (SMLA) per group from 2 independent experiments; For (c-d), data are mean  $\pm$  s.e.m. **e-i**, *Ccr2*<sup>RFP/wt</sup> mice were infected with low-dose *S. aureus* bead, treated with vehicle or leptin, and imaged at 14 days post-infection. **e**, Experiment timeline showing leptin treatment to *Ccr2*<sup>RFP/wt</sup> mice. **f**, Representative images showing effect of leptin treatment on blood vasculature in *Ccr2*<sup>RFP/wt</sup> mice at 14 d post-infection. Top: 2D stitch of wound, bottom: 3D projection of vasculature. Scale bars, 300  $\mu\text{m}$  (top) and 100  $\mu\text{m}$  (bottom). Images representative of  $n = 8$  mice (vehicle) and 9 mice (leptin) per group from

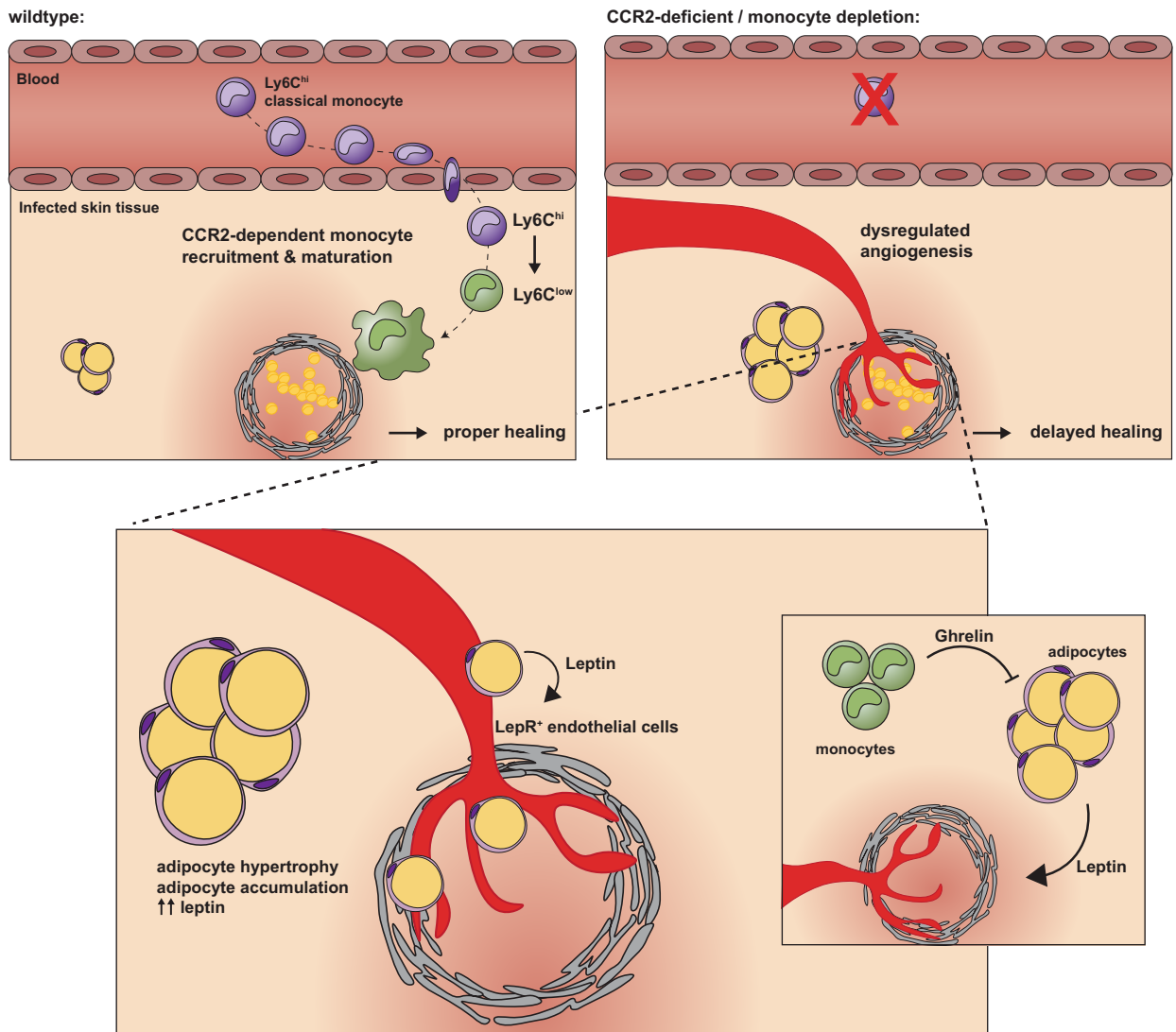
2 independent experiments. **g**, Quantification of blood vasculature.  $n = 4$  per group from 2 independent experiments; unpaired two-sided Student *t*-test; data are mean  $\pm$  s.e.m.;  $P = 0.0310$ . **h**, Quantification of wound presence.  $n = 8$  mice (vehicle) and 9 mice (leptin) per group from 2 independent experiments. **i**, Quantification of wound size.  $n = 4$  per group from 2 independent experiments; unpaired two-sided Student *t*-test; data are mean  $\pm$  s.e.m.;  $P = 0.0571$ . **j-m**, *Ccr2*<sup>RFP/RFP</sup> mice were infected with low-dose *S. aureus* bead, treated with vehicle or leptin, and imaged at 14 days post-infection. **j**, Experiment timeline for leptin administration to *Ccr2*<sup>RFP/RFP</sup> mice infected with *S. aureus* bead. **k**, Quantification of wound presence. **l**, Quantification of vasculature volume. Data are mean  $\pm$  s.e.m. **m**, Quantification of wound size. Data are mean  $\pm$  s.e.m. For (k-m),  $n = 6$  mice (vehicle) and  $n = 4$  mice (leptin) from 2 independent experiments.



**Extended Data Fig. 9 | Leptin-Lepr signaling drives vasculature formation during *S. aureus* skin infection.** **a**, Uniform Manifold Approximation and Projection (UMAP) of single cells isolated from murine back skin. **b–e**, UMAP showing expression of *Pecam1* (**b**), *Lyve1* (**c**), *Flt1* (**d**) and *Lepr* (**e**). **f**, Violin plot showing *Lepr* expression. **g–k**, Tamoxifen-treated *LepR<sup>fl/fl</sup>* *Cdh5(PAC)-CreERT2* and *LepR<sup>fl/fl</sup>* control mice were treated with MC-21, infected with *S. aureus* bead, and imaged at 14 d post-infection. **g**, Experiment timeline for tamoxifen treatment, MC-21 administration, infection, and imaging. **h**, Representative images at 14 d post-infection. Top: 2D stitch of entire wound, bottom: 3D projection of vasculature. Scale bars, 200  $\mu$ m. Images representative of  $n = 7$  per group from 2 independent experiments. **i**, Quantification of wound presence.  $n = 7$  per group from 2 independent experiments. **j**, Quantification of vasculature volume.  $n = 7$  per group from 2 independent experiments; unpaired two-sided Student *t*-test; data are mean  $\pm$  s.e.m.;  $P = 0.0180$ . **k**,

Quantification of wound size.  $n = 7$  per group from 2 independent experiments; unpaired two-sided Student *t*-test; data are mean  $\pm$  s.e.m.;  $P = 0.0425$ . **l**, Quantification of wound size at 14 d post-infection in *Ccr2<sup>RFP/RFP</sup>* mice after vehicle or ghrelin treatment.  $n = 6$  (vehicle) and  $n = 9$  (ghrelin) from 2 independent experiments. Data are mean  $\pm$  s.e.m. **m–p**, *Ccr2<sup>RFP/+</sup>* mice were infected with low-dose *S. aureus* bead, treated with vehicle or ghrelin, and imaged at 14 days post-infection. **m**, Experiment timeline showing ghrelin treatment to *Ccr2<sup>RFP/+</sup>* mice. **n**, Quantification of wound presence.  $n = 10$  per group from 2 independent experiments; two-sided Chi-squared test;  $P = 0.0191$ . **o**, Quantification of vasculature volume.  $n = 9$  mice (vehicle) and  $n = 4$  mice (ghrelin) from 2 independent experiments; data are mean  $\pm$  s.e.m. **p**, Quantification of wound size.  $n = 10$  per group from 2 independent experiments; data are mean  $\pm$  s.e.m.

# A monocyte-leptin-angiogenesis pathway critical for repair post infection



**Extended Data Fig.10 | Model for the role of monocytes during *S. aureus* skin infection.** Monocytes are recruited in a CCR2-dependent manner to a low-dose *S. aureus* skin infection to regulate tissue by limiting leptin-mediated angiogenesis through local production of ghrelin. In CCR2-deficient mice, or

after anti-CCR2 monocyte depletion, there is no monocyte recruitment to the skin infection, which results in pathologic angiogenesis driven by leptin and delayed healing. Monocytes function as a cellular rheostat by regulating leptin levels and revascularization during tissue repair post-infection.

## Reporting Summary

Nature Portfolio wishes to improve the reproducibility of the work that we publish. This form provides structure for consistency and transparency in reporting. For further information on Nature Portfolio policies, see our [Editorial Policies](#) and the [Editorial Policy Checklist](#).

### Statistics

For all statistical analyses, confirm that the following items are present in the figure legend, table legend, main text, or Methods section.

- | n/a                                 | Confirmed  |
|-------------------------------------|--|
| <input type="checkbox"/>            | <input checked="" type="checkbox"/> The exact sample size ( $n$ ) for each experimental group/condition, given as a discrete number and unit of measurement  |
| <input type="checkbox"/>            | <input checked="" type="checkbox"/> A statement on whether measurements were taken from distinct samples or whether the same sample was measured repeatedly  |
| <input type="checkbox"/>            | <input checked="" type="checkbox"/> The statistical test(s) used AND whether they are one- or two-sided<br><i>Only common tests should be described solely by name; describe more complex techniques in the Methods section.</i>   |
| <input checked="" type="checkbox"/> | <input type="checkbox"/> A description of all covariates tested  |
| <input type="checkbox"/>            | <input checked="" type="checkbox"/> A description of any assumptions or corrections, such as tests of normality and adjustment for multiple comparisons  |
| <input type="checkbox"/>            | <input checked="" type="checkbox"/> A full description of the statistical parameters including central tendency (e.g. means) or other basic estimates (e.g. regression coefficient) AND variation (e.g. standard deviation) or associated estimates of uncertainty (e.g. confidence intervals) |
| <input type="checkbox"/>            | <input checked="" type="checkbox"/> For null hypothesis testing, the test statistic (e.g. $F$ , $t$ , $r$ ) with confidence intervals, effect sizes, degrees of freedom and $P$ value noted<br><i>Give <math>P</math> values as exact values whenever suitable.</i>                            |
| <input checked="" type="checkbox"/> | <input type="checkbox"/> For Bayesian analysis, information on the choice of priors and Markov chain Monte Carlo settings  |
| <input checked="" type="checkbox"/> | <input type="checkbox"/> For hierarchical and complex designs, identification of the appropriate level for tests and full reporting of outcomes  |
| <input checked="" type="checkbox"/> | <input type="checkbox"/> Estimates of effect sizes (e.g. Cohen's $d$ , Pearson's $r$ ), indicating how they were calculated  |

*Our web collection on [statistics for biologists](#) contains articles on many of the points above.*

### Software and code

Policy information about [availability of computer code](#)

Data collection	LasX (v3.5.5.19976 for confocal and v3.5.7.23225 for multiphoton), NIS-Elements AR 5.30.05 (Build 1559), QuantStudio 6 Flex Real-Time PCR Systems, SpectroFlow (v3.0.3, 11292021), CytExpert (v2.4), XL30, ESEM (Philips), Olympus cellSens Standard 1.18 (Build 16686), BDFACSDiva (v8.0.2), Micro-Manager 2.0.0 (Open Source Microscopy Software), Volocity image acquisition software (v6.1.1).
Data analysis	Imaris (v9.5), MATLAB (vR2022a), ImageJ (v2.1.0), FlowJo (v10), R/RStudio (v1.3.1093), Prism Graphpad (v9.1.1), Microsoft® Excel® for Microsoft 365 MSO (v2205 Build 16.0.15225.20028)

For manuscripts utilizing custom algorithms or software that are central to the research but not yet described in published literature, software must be made available to editors and reviewers. We strongly encourage code deposition in a community repository (e.g. GitHub). See the Nature Portfolio [guidelines for submitting code & software](#) for further information.

### Data

Policy information about [availability of data](#)

All manuscripts must include a [data availability statement](#). This statement should provide the following information, where applicable:

- Accession codes, unique identifiers, or web links for publicly available datasets
- A description of any restrictions on data availability
- For clinical datasets or third party data, please ensure that the statement adheres to our [policy](#)

The single cell RNA sequencing dataset analyzed in the this study is available in the Gene Expression Omnibus repository under accession code GSM2910020

## Field-specific reporting

Please select the one below that is the best fit for your research. If you are not sure, read the appropriate sections before making your selection.

Life sciences  Behavioural & social sciences  Ecological, evolutionary & environmental sciences

For a reference copy of the document with all sections, see [nature.com/documents/nr-reporting-summary-flat.pdf](https://www.nature.com/documents/nr-reporting-summary-flat.pdf)

## Life sciences study design

All studies must disclose on these points even when the disclosure is negative.

Sample size	In most experiments sample size was determined based on previous studies within the lab using these techniques. For intravital microscopy, we were limited by imaging only one mouse at a time so a minimum of 1 experimental mouse and 1 control mouse was imaged per day. Sample size was determined based on prior studies and literature using similar experimental paradigms (Wang et al., Science, 2017; Zindel et al., Science, 2021; Neupane et al., Cell, 2020). In instances where the approach had not previously been used, a minimum of 4 animals/group were utilized.
Data exclusions	No data was excluded.
Replication	All experiments were replicated at least once with similar findings and all replications were successful.
Randomization	For all experiments that required either pharmacological treatment or different infection conditions, mice were randomized.
Blinding	The investigators were not blinded during experiments because treatments and data collection were performed by the same researcher. For image analysis, the images were randomly assigned a key by the researcher and all images were processed using the same workflow, therefore, image analysis was blinded after data collection.

## Reporting for specific materials, systems and methods

We require information from authors about some types of materials, experimental systems and methods used in many studies. Here, indicate whether each material, system or method listed is relevant to your study. If you are not sure if a list item applies to your research, read the appropriate section before selecting a response.

### Materials & experimental systems

n/a	Involved in the study
<input type="checkbox"/>	<input checked="" type="checkbox"/> Antibodies
<input checked="" type="checkbox"/>	<input type="checkbox"/> Eukaryotic cell lines
<input checked="" type="checkbox"/>	<input type="checkbox"/> Palaeontology and archaeology
<input type="checkbox"/>	<input checked="" type="checkbox"/> Animals and other organisms
<input checked="" type="checkbox"/>	<input type="checkbox"/> Human research participants
<input checked="" type="checkbox"/>	<input type="checkbox"/> Clinical data
<input checked="" type="checkbox"/>	<input type="checkbox"/> Dual use research of concern

### Methods

n/a	Involved in the study
<input checked="" type="checkbox"/>	<input type="checkbox"/> ChIP-seq
<input type="checkbox"/>	<input checked="" type="checkbox"/> Flow cytometry
<input checked="" type="checkbox"/>	<input type="checkbox"/> MRI-based neuroimaging

## Antibodies

### Antibodies used

antibody / clone / fluorophore / dilution factor / supplier name / catalog # / lot #  
 Rat Anti-Mouse Mer / 108928 / BUV 395 / 40 / BD / 747897 / 1050224  
 Rat Anti-Mouse CD8a / 53-6.7 / BUV496 / 80 / BD / 750024 / 1250565  
 Rat Anti-Mouse TIM-4 / 21H12 / BUV 661 / 80 / BD / 750205 / 1208138  
 Rat anti-mouse CD170 (Siglec F) / 1RNM44N / BUV737 / 80 / BD / 750024 / 2418738  
 Hamster Anti-Mouse CD11c / HL3 / BUV 805 / 40 / BD / 749090 / 1250562  
 Rat Anti-Mouse CD45R/B220 / RA3-6B2 / BV421 / 160 / BD / 562922 / 1177098  
 Rat anti-mouse MHC Class II (I-A/I-E) / M5/114.15.2 / eFluor 450 / 320 / Invitrogen / 48-5321-80 / 2065669  
 Rat Anti-Mouse CD19 / 1D3 / BV480 / 160 / BD / 566167 / 2006246  
 Rat anti-mouse CD45 / 30-F11 / BV510 / 320 / BioLegend / 103138 / B338490  
 Mouse anti-mouse NK-1.1 / PK136 / BV570 / 53.3 / BioLegend / 108733 / B346179  
 Rat anti-mouse CD206 (MMR) / C068C2 / BV605 / 40 / BioLegend / 141721 / B325745  
 Rat Anti-Mouse Ly-6G / 1A8 / BV650 / 80 / BD / 740554 / 1099578  
 Mouse anti-mouse CX3CR1 / SA011F11 / BV711 / 160 / BioLegend / 149031 / B336006  
 Rat anti-mouse/human CD11b / M1/70 / BV750 / 800 / BioLegend / 101267 / B340388  
 Rat anti-mouse CD192 (CCR2) / sA203G11 / BV786 / 160 / BioLegend / 150621 / B303782  
 Armenian Hamster anti-mouse CD3ε / 145-2C11 / PerCP / 40 / BioLegend / 100325 / B312428  
 Rat anti-mouse Ly-6C / HK1.4 / PerCP-Cy5.5 / 320 / BioLegend / 129012 / B282011  
 Mouse anti-Mouse CD64 a and b Alloantigens / X54-5/7.1 / Alexa Fluor 647 / 160 / BD / 558539 / 30911



84%A2%20750%20anti-mouse%20CD24%20Antibody.pdf  
 Rat anti-mouse CD4 / GK1.5 / APC/Fire 810 / BioLegend / 100479 / <https://www.biolegend.com/it-it/products/apc-fire-810-anti-mouse-cd4-antibody-19552?pdf=true&displayInline=true&leftRightMargin=15&topBottomMargin=15&filename=APC/Fire%E2%84%A2%20810%20anti-mouse%20CD4%20Antibody.pdf>  
 Rat Anti-Mouse F4/80 / T45-2342 / PE-CF594 / BD / 565613 / [https://www.bdbiosciences.com/content/dam/bdb/products/global/reagents/flow-cytometry-reagents/research-reagents/single-color-antibodies-ruo/565613\\_base/pdf/565613.pdf](https://www.bdbiosciences.com/content/dam/bdb/products/global/reagents/flow-cytometry-reagents/research-reagents/single-color-antibodies-ruo/565613_base/pdf/565613.pdf)  
 Armenain Hampster anti-mouse TCR gamma/delta / eBioGL3 / PE-Cy5 / eBiosciences / 15-5711-82 / [https://www.thermofisher.com/order/genome-database/dataSheetPdf?producttype=antibody&productssubtype=antibody\\_primary&productId=15-5711-82&version=230](https://www.thermofisher.com/order/genome-database/dataSheetPdf?producttype=antibody&productssubtype=antibody_primary&productId=15-5711-82&version=230)  
 Rat anti-mouse CD16/CD32 / 2.4G2 / - / Bio X Cell / BE0307 / <https://d2a7cdyquyl45u.cloudfront.net/tds-sheets/BE0307-tds.pdf>  
 rabbit anti-mouse leptin / polyclonal / - / abcam / ab16227 / <https://www.abcam.com/leptin-antibody-ab16227.html>  
 rabbit IgG polyclonal isotype control / polyclonal / - / abcam / ab171870 / <https://www.abcam.com/rabbit-igg-polyclonal-isotype-control-chip-grade-ab171870.html>  
 goat pAb to rabbit IgG secondary / polyclonal / AF488 / abcam / ab150077 / <https://www.abcam.com/goat-rabbit-igg-hl-alex-fluor-488-ab150077.html>  
 Rat anti-mouse Ly6G (depleting antibody) / 1A8 / - / Bio X Cell / BE0075-1 / <https://d2a7cdyquyl45u.cloudfront.net/tds-sheets/BE0075-1-tds.pdf>  
 Rat IgG2a isotype control / 2A3 / - / Bio X Cell / BE0089 / <https://d2a7cdyquyl45u.cloudfront.net/tds-sheets/BE0089-tds.pdf>  
 Rat anti-mouse CCR2 (depleting antibody) / MC-21 / - / Prof. Mathias Mack / 1480/02 / Mack, M. et al. Expression and characterization of the chemokine receptors CCR2 and CCR5 in mice. *J Immunol* 166, 4697-4704 (2001).  
 Rat IgG2a isotype control / MC-67 / - / Prof. Mathias Mack / 481/02 / Mack, M. et al. Expression and characterization of the chemokine receptors CCR2 and CCR5 in mice. *J Immunol* 166, 4697-4704 (2001).  
 rabbit polyclonal anti-perilipin-1 / polyclonal / - / Abcam / ab3526 / <https://www.abcam.com/perilipin-1-antibody-ab3526.html>  
 donkey anti-rabbit IgG / polyclonal / AF588 / Jackson Immunoresearch Labs / 711-545-152 / <https://www.jacksonimmuno.com/catalog/products/711-545-152>  
 goat anti-rabbit IgG / polyclonal / Cy5 / Jackson Immunoresearch Labs / 111-175-008 / <https://www.jacksonimmuno.com/catalog/products/111-175-144>

## Animals and other organisms

Policy information about [studies involving animals](#); [ARRIVE guidelines](#) recommended for reporting animal research

### Laboratory animals

Animal experiments were performed with adult male and female 7-8-wk-old mice and all experimental animal protocols were approved by the University of Calgary Animal Care Committee and followed guidelines established by the Canadian Council for Animal Care (protocol number AC19-0138). All mice were housed under a 12/12 light/dark cycle at 22-25°C and 30-70% humidity under specific pathogen-free conditions. Mice received sterilized rodent chow and water ad libitum. Mice infected longer than 24 hours were stored in a biohazard facility biosafety level 2. C56BL/6, CX3CR1gfp/wt, and CX3CR1gfp/gfp mice were purchased from The Jackson Laboratory and bred in house. Ly6G-cre/Ai14 (CatchupIVM-red) mice were a kind gift from Matthias Gunzer. We crossed CatchupIVM-red mice to CX3CR1gfp/gfp mice to generate CatchupIVM-red CX3CR1gfp/wt double reporter mice. Generation of CCR2rfp/rfp (CCR2-deficient) and CCR2rfp/wt (knock-in) mice have been previously described<sup>27</sup>. CX3CR1gfp/wt CCR2rfp/wt were generated by crossing CX3CR1gfp/gfp CCR2rfp/rfp mice with C57BL/6 mice. CCR2creERT2 zsGreen+/- were a kind gift from Dr. Nathan Peters, made by Dr. Burkhard Becher. WT and Ghrl-/- bones were sent to us from Yuxiang Sun to set up bone marrow transfers into C57 mice. LepRf/fl were a kind gift from Dr. Timothy Kieffer. Cdh5(PAC)CreERT2 were from Taconic. We bred the LepRf/fl to Cdh5(PAC)CreERT2 mice to generate LepRf/fl Cdh5(PAC)CreERT2+ mice and LepRf/fl littermate controls.

### Wild animals

no wild animals were used in this study.

### Field-collected samples

no field-collected samples were used in this study.

### Ethics oversight

All experimental animal protocols were approved by the University of Calgary Animal Care Committee and followed guidelines established by the Canadian Council for Animal Care (protocol number AC19-0138).

Note that full information on the approval of the study protocol must also be provided in the manuscript.

## Flow Cytometry

### Plots

Confirm that:

- The axis labels state the marker and fluorochrome used (e.g. CD4-FITC).
- The axis scales are clearly visible. Include numbers along axes only for bottom left plot of group (a 'group' is an analysis of identical markers).
- All plots are contour plots with outliers or pseudocolor plots.
- A numerical value for number of cells or percentage (with statistics) is provided.

### Methodology

#### Sample preparation

Cells were prepared for single cell suspension from skin infections as outlined in method section:

Skin biopsies of the infected area were harvested (1 cm<sup>2</sup> section) and collected into cold HBSS. Skin tissue was digested as previously described<sup>34</sup>. Skin tissue was incubated at 37°C with gentle rotation for 75 minutes in 2 mL of HBSS containing 3%

	<p>FBS, 5 mM EDTA and 0.8 mg/mL collagenase II (Worthington). Following enzymatic digestion tissue was passed through a 70 <math>\mu</math>m filter and washed with HBSS containing 3% FBS and 5 mM EDTA. A debris removal step was performed as per manufacturer protocol in the debris removal kit (Miltenyi Biotech). Single cells were resuspended in 800 <math>\mu</math>L of HBSS containing 3% FBS and 5 mM EDTA and 200 <math>\mu</math>L was used for antibody staining. Blood was obtained by intra-cardiac bleed and red blood cells were lysed with ACK lysing buffer.</p> <p>Antibody staining of surface-expressed molecules were performed as described. Cells were first stained with Fc blocking antibody (1:200) and Ghost Red 710 fixable viability dye (1:6400) in HBSS for 30 minutes on ice. CCR2 antibody staining was done at 37°C for 20 minutes. Next, cell suspensions were stained for remaining surface antigens in HBSS supplemented with 3% FBS and 5 mM EDTA for 20 minutes on ice. When indicated, CX3CR1gfp/wt CCR2rfp/wt transgenic reporter mice were used for identifying monocyte subsets using flow cytometry. After washing with HBSS containing 3% FBS and 5 mM EDTA, cells were fixed with 1% paraformaldehyde in HBSS for 15 minutes on ice and then run the following day on the Cytoflex flow cytometer or Cytex spectral cytometer. All flow cytometry experiments were analyzed with FlowJo v10 (Tree Star).</p>
Instrument	Cytoflex LS (Beckman Coulter), Cytex Aurora
Software	Samples were acquired on the Cytoflex LS (Beckman Coulter) with software SpectroFlow (v3.0.3, 11292021), FACS Aria (BD) with software BDFACSDiva version 8.0.2, and Cytex Aurora with software CytExpert (v2.4). Flow cytometry data was analyzed using FlowJo version 10 (TreeStar).
Cell population abundance	The skin infection/wound contained a large abundance of cells early during the inflammatory phase of infection, but during wound repair at 14 days post infection there were fewer cells recovered. Cells were counted using a hemocytometer during flow cytometry preparation and approximately $2 \times 10^6$ cells total were stained with surface antibodies, or if there were fewer cells recovered, the entire sample was used for flow cytometry. Counting beads were used to quantify total numbers of cells.
Gating strategy	Gating strategy is outlined in Extended Data Fig. 3. Briefly, Live, singlet cells were identified as (1) neutrophils (CD45+CD11b+Ly6G+Ly6Cint), (2) Ly6Chi monocytes (CD45+CD11b+Ly6G-Ly6ChiCD64low/+), (3) Ly6Clow monocytes (CD45+CD11b+Ly6G-Ly6ClowCD64+), (4) P1 monocytes (CD45+CD11b+Ly6G-Ly6Clow-hiCD64low-hiCCR2+Ly6ChiMHCIllow), (5) P2 monocytes/macrophages (CD45+CD11b+Ly6G-Ly6Clow-hiCD64low-hiCCR2+Ly6ChiMHCIlhi), (6) P3 monocytes/macrophages (CD45+CD11b+Ly6G-Ly6Clow-hiCD64low-hiCCR2+Ly6ClowMHCIlhi), (7) P4 dermal macrophages (CD45+CD11b+Ly6G-Ly6Clow-hiCD64low-hiCCR2-Ly6ClowMHCIllow), (8) P5 dermal macrophages (CD45+CD11b+Ly6G-Ly6Clow-hiCD64low-hiCCR2-Ly6ClowMHCIlhi), (9) CD4 T cells (CD45+Ly6G-CD11b-CD3e+CD4+), (10) CD8 T cells (CD45+Ly6G-CD11b-CD3e+CD8+), (11) $\gamma\delta$ T cells (CD45+Ly6G-CD11b-CD3e+CD4-CD8-TCR $\gamma\delta$ +), (12) B cells (CD45+Ly6G-CD11b-CD3e-CD45R+CD19+), (13) NK cells (CD45+Ly6G-CD11b-CD3e-CD45R-CD19-NK1.1+), and (14) Lineage- (CD45+Ly6G-CD11b-CD3e-CD45R-CD19-NK1.1-).

Tick this box to confirm that a figure exemplifying the gating strategy is provided in the Supplementary Information.